Experimental study of open-channel flow and turbulence over roughness elements

Jing Li

A thesis in

The Department of

Building, Civil and Environmental Engineering

Presented in Partial Fulfilment of the Requirements

for the Degree of Master of Applied Science in Civil Engineering at

Concordia University

Montreal, Quebec, Canada

January 2019

CONCORDIA UNIVERSITY

School of Graduate Studies

This is to certify that the thesis prepared

By: Jing Li

Entitled Experimental study of open-channel flow and turbulence over roughness elements

and submitted in partial fulfillment of the requirements for the degree of

Master of Applied Science (Civil Engineering)

Complies with the regulations of Concordia University and meets the accepted standards with respect to originality and quality.

Signed by the final examining committee:

Dr. Catherine N. Mulligan Chair

Dr. F. Nasiri Examiner

Dr. M. Kheiri Examiner

Dr. S. Samuel Li Supervisor

Approved by _____

_____

Date _____

ABSTRACT

Experimental study of open-channel flow and turbulence over roughness elements

Jing Li

It is common that open-channel flows are turbulent and the channel-bed surfaces are rough. The presence of roughness elements on the channel-bed has significant influences on the flow characteristics in the bed vicinity and further above. Some earlier researchers have created two-dimensional roughness in laboratory channels by placing rectangular ribs on the bed and three-dimensional roughness by gluing sediment grains of irregular shape on the bed. Elements in the form of cubes are arguably more suitable to quantify the influences. However, laboratory experiments for detailed measurements of flow velocity and turbulence over cubical elements are rarely available. In this thesis, laboratory experiments of turbulent flow over acrylic cubes in a rectangular channel were carried out. Cubes with sides of 1.905 cm (3/4 inches) are uniformly mounted as roughness elements on the horizontal bed. The approach flow depth ranges from 8.8 to 9.1 cm or 4.62 to 4.78 times the roughness height. The experiments cover three conditions of cube spacing: being 2, 4, and 6 times the cube side dimensions; these relative spacing conditions represent the d-type, intermedium-type, and k-type roughness, respectively. Using an acoustic Doppler velocimeter (ADV), detailed measurements of three-dimensional flow velocities and turbulence quantities were made at locations above and around the cubes. At each location, the measurements lasted 60 s, at a sampling frequency of 120 Hz. The positions of the ADV probe were controlled accurately (± 1 mm) by a step motor. The velocity distributions are shown to be much more complex than the boundary-layer velocity distributions widely used in the literature. We categorized vertical profiles of the longitudinal velocity component into six distinct types (types 1 – 6) and vertical profiles of turbulent shear stress into five types (types 1 – 5). Based on measurements of the longitudinal velocity component and turbulent shear stress, we calculated velocity distributions for the d-type roughness by using the logarithmic law. There are large discrepancies between the calculation results and measurements. Moreover, we obtained contours of the secondary flow intensity in various planes. The distributions of the secondary flow are symmetrical with respect to the channel centreline at some cross sections but asymmetrical at other

cross sections. The k-type roughness is shown to produce stronger secondary flow than the d-type and intermediate type of roughness. The experimental results are useful for model validations.

Contents

A List of Symbols

The following symbols have been used in this thesis:

L_e	entrance length (m)
u_*	friction velocity (m/s)
U_s	intensity of secondary flow (%)
$\bar{u}$	Reynolds average velocity component in the *x*-direction (m/s)
$\bar{v}$	Reynolds average velocity component in the *y*-direction (m/s)
$\bar{w}$	Reynolds average velocity component in the *z*-direction (m/s)
z_0	constant of integration
τ_{xz}	Reynolds stress (N/m^2)
A	small surface (m^2)
D	the diameter of the pipeline
h	roughness height
H	water depth
k	roughness height (m)
L	crest-to-crest distance, or distance between the centerlines of two consecutive cubes (m)
l	mixing length (m)
N	constant, equal to 21600
Q	flow discharge (L/s)
R	hydraulic radius
Re	Reynolds number
U	flow velocity
u	instantaneous velocity component in the *x*-direction (m/s)

v	instantaneous velocity component in the *y*-direction (m/s)
w	instantaneous velocity component in the *z*-direction (m/s)
x	longitudinal coordinates (m)
y	lateral coordinates (m)
y^+	wall distance
z	vertical coordinates (m)
Δy	lateral spacing (m)
κ	von Kármán constant (= 0.41)
ν	kinematic viscosity of water (m^2/s)
ρ	density of water
τ	turbulent shear stress (N/ m^2)
τ_b	bed shear stress (N/ m^2)
m	constant, equal to 1/9 or 1/30

A List of figures

The following figures have been used in this thesis:

A List of Tables

The following tables have been used in this thesis:

Chapter 1 Introduction

1.1 Background

The channel-bed of a natural open-channel including rivers, canals and streams is commonly a rough surface (Figure 1.1). The flow of water over a rough bed surface is turbulent. There have been numerous cases where turbulent open-channel flow exerts large shear stresses on the bed and erodes bed sediments. Erosion of bed sediments can cause severe damage to fish habitats. The eroded sediments are deposited to channel sections downstream. This can lead to river floods and navigation hazards. Clearly, the study of turbulent flow in the vicinity of a rough bed surface is of ecological and environmental relevance. Currently, there is a deficit of knowledge about near-bed turbulent flow.

Figure 1.1 Photo of turbulent flow in a gravel-bed river channel with a rough channel-bed (used with permission from Kirstie Fryirs).

In fact, many different types of man-made channels in hydraulic engineering applications have a rough channel-bed. Examples of these channels include hydropower channels for energy generation, irrigation channels for agricultural development and food production, water supply channels for human consumption and industrial use, and drainage channels for prevention of urban floods. The bed surfaces of such channels are almost always a concrete surface that is made smooth and is nonerodible. However, due to abrasion of concrete materials and fouling after a certain time period of service life, the smooth bed-surface can become a rough surface. In order to understand the hydraulic performance of these engineering channels, we need to study the problem of turbulent flow over surface roughness.

The topic of turbulent flow over surface roughness has attracted increasing research attention in the past. Chow (1959) introduced three types of surface roughness and discussed the dynamic effect of surface roughness in the near-bed region. The author suggested that the behaviours of the turbulent boundary layer above a rough bed differ from that above a smooth bed. A good understanding of the behaviours entails detailed measurements from the near-bed region under rough condition. Chow (1959) classified three types of flow over surface roughness:

1) quasi-smooth flow, which is over a bed surface with closely spaced roughness elements at the bed;
2) wake-interference flow, which is over a bed surface with relatively closely spaced roughness elements at the bed; and
3) isolated-roughness flow, which is over a bed surface with largely spaced roughness elements.

Perry et al. (1969) conducted laboratory experiments in pipes to investigate hydraulic behaviours in the near-wall region, and categorized surface roughness into two types: 1) the d-type roughness elements with close spacing, and 2) the k-type roughness with large spacing.

After the 1990, researchers started to quantify different surface roughness and their effects. They used bars and spheres of regular shapes in experiments of flow to model surface roughness. Most of the studies followed Perry's (1969) work, and continued using the terms of the d-type roughness and the k-type roughness. In addition, the researchers introduced another roughness type, called the intermediate type (or transitional type). For examples, Agelinchaab and Tachie (2006) used hemispherical ribs to investigate the characteristics of flow over the k-type, intermediate type and the d-type surface roughness. Coleman et al. (2007) used square ribs as roughness elements to model the k-type, intermediate type and the d-type roughness. Manes et al. (2007) used spheres as surface roughness to investigate the d-type roughness. Cameron et al. (2008) used spheres as roughness elements to investigate intermediate surface roughness. These studies produced measurements in the near-bed region. However, because of the geometry of the roughness elements used, most of the studies mentioned above observed turbulent flow structures under the limit of two dimensions. The third dimension is missing. It is desirable to obtain three-dimensional measurements of turbulent flow structures around roughness elements.

The most recent experimental study of turbulent flow over roughness surface was reported in Singh et al. (2017). Used wooden cubes as roughness elements, they investigated three types of surface roughness and measured near-bed velocities above and around the elements. They assumed that the flow structure would be symmetrical about a vertical plane at the centreline of the channel. As a result, they made measurements of flow velocities from only one side of the centreline. There were significant uncertainties in the simplification of one-sided measurements. The authors

applied double-averaged method to estimate shear stress distributions. Their work was discussed in Li and Li (2018).

In summary, we have recognised a lack of three-dimensional measurements of flow velocities over surface roughness. This has led to the current research work. We carried out laboratory experiments of flow over acrylic cubes in order to achieve a better understanding of the impact of different surface roughness on the flow field.

1.2 Objectives of this study

The main objective of this research work is to understand the effect of surface roughness on turbulent flow in open-channels. The specific aims are to:

- measure three-dimensional flow velocities from the near-bed region under conditions of different types of surface roughness;
- quantify the structures of the primary flow as well as secondary flow over the three types of surface roughness;
- estimate distributions of turbulent shear stresses under conditions of the three types of surface roughness; and
- examine the differences of measured flow velocity profiles from widely used theoretical velocity profiles.

1.3 Significance of this study

The topic of turbulent flow over surface roughness is a fundamental topic in hydraulic engineering. It has a wide range of important applications. Experimental results of turbulent flow over surface roughness are very limited. The significance of this experimental research is emphasised below:

1) This experimental work has produced detailed measurements of near-bed flow velocities in three orthogonal directions. Near-bed flow velocities are very notoriously difficult to measure from laboratory experiments, which is part of the reason that such measurements are rarely available in the literature.
2) This work made measurements systematically, covering different types of surface roughness and a large volume of measurement locations (1,200 measurement points). The spatial resolutions and accuracy of positions are high. This is critical to understanding the spatial distributions of turbulent flow variables.
3) The sampling frequency (or temporal resolutions) of flow velocity components is high. This enables us to obtain turbulence shear stresses and other turbulence quantities.
4) This experimental study represents a significant extension of the previous studies of the topic, which used rectangular bars, spheres and gravels as rough elements in open-channel flows.

Overall, this experimental study makes a good contribution to an improved understanding of the characteristics of turbulent flow near a rough bed surface. The measurements of flow velocities and shear stresses from this study are useful for calibration and validation of numerical models. The numerical models, in turn, may be used to improve the design of man-made open-channels, to investigate effective ways of controlling sediment erosion in natural open-channels, and to protect the health of fish habitats.

1.4 Overview of this thesis

The remaining part of this thesis is organised as follows: Chapter 2 gives a critical review of the pertinent literature. It covers near-bed turbulence, surface roughness, flow velocity distributions under smooth- and rough-bed conditions, the concept of the law-of-the-wall, and the concept of secondary flow.

Chapter 3 begins with explanations of the experimental setup in the Hydraulics Laboratory used in this study. It proceeds to discuss the creation of roughness surfaces and strategies to achieve accurate positions of flow velocity measurements. This is followed by a description of the acoustic Doppler velocimeter (ADV) setup, configurations and data processing. The last section of Chapter 3 discusses the hydraulic conditions of the experiments.

Chapter 4 is devoted to presentations of the experimental results. In this chapter, we begin with the vertical structures of the primary flow in the longitudinal direction, followed by the inflow to and outflow from cavities between roughness elements. Then, we cover the horizontal and vertical distributions of secondary flow. Toward the end of this chapter, the distribution of Reynolds shear stresses is discussed, along with comparisons of measured mean velocity profiles to classic theoretical velocity distributions.

Chapter 5 provides conclusions drawn from this experimental study, and suggestions for further studies of the topic of turbulent flow over surface roughness.

Chapter 2 Literature Review

This chapter provides a review of the literature about the structures of mean flow in an open-channel, different types of roughness surface, and turbulence characteristics of open-channel flow. These characteristics include distributions of flow velocity, the Reynolds shear stress, and secondary flow.

2.1 Three types of roughness surface (channel-bed)

Natural open-channels commonly have an irregular bed surface that is rough. An example of such surfaces is shown in Figure 1.1. In this example, the rough surface consists of gravel of different sizes and irregular shapes. They are termed roughness elements in this research thesis. Their presence at the bed surface has profound effects on the flow of water over the bed surface.

Chow (1959) simplified irregular surface roughness as individual roughness elements of regular shape (Figure 2.1). The author categorised surface roughness into three types:

- quasi-smooth roughness;
- wake-interference roughness; and
- isolated roughness.

For quasi-smooth roughness, the roughness elements are closely placed, vortices at one cube completely develop and occupy the whole cavity between two consecutive cubes. The roughness elements have minimum influence on the flow in the outer layer of the water column above the roughness elements.

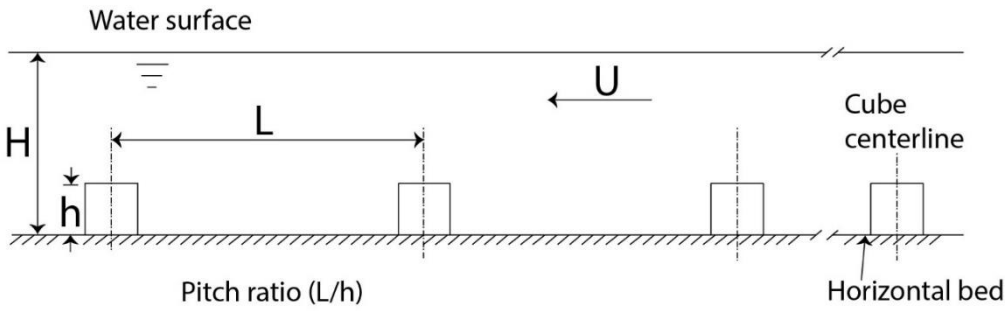

Figure 2.1 Side view of flow over surface roughness, where H is the water depth, and U is flow velocity.

For isolated roughness, the roughness elements have relatively large spacing between any two consecutive roughness elements. Vortices at one element form and completely develop upstream of the next cube. The roughness elements significantly affect the outer layer of water column.

For wake-interference roughness, the roughness elements have moderate spacing. Vortices occurring at one element mix into the vortices at the next cube at downstream. The roughness elements influence the flow in the outer layer of the water column.

Perry et al. (1969) reviewed previous studies of roughness effects on pipe flow (Figure 2.2) and summarised observational evidences from experiments involving a roughen surface with densely spaced roughness elements. Perry et al. (1969) conducted experiments that involved the so-called d-type and k-type of surface roughness. The authors investigated the impact of surface roughness on turbulent flow behaviours. According to Perry et al. (1969), the d-type of surface roughness means $L/h \leq 2$, whereas the k-type of surface roughness means $L/h \geq 6$, where h is the roughness height, and L is the crest-to-crest distance (Figure 2.1).

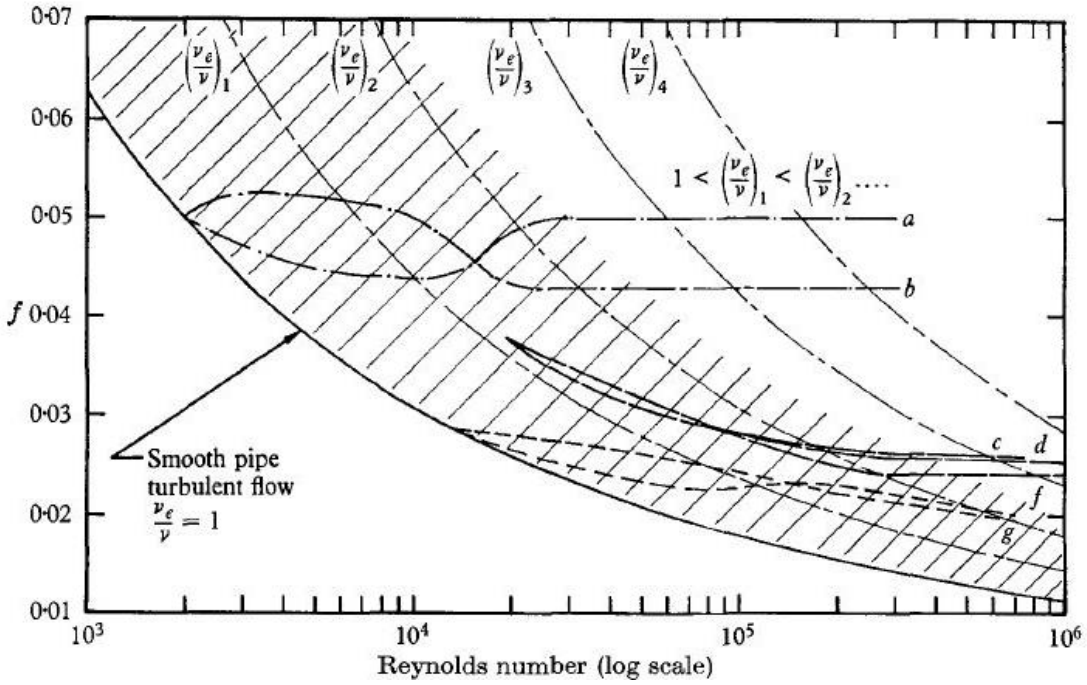

Figure 2.2 Flow over the d-type roughness in rough pipes of different h/d values: a) k/D = 0.0125 (Sams, 1952); b) k/D = 0.0185 (Sams, 1952); c) k/D = 0.0204 (Streeter and Chu, 1949); d) k/D = 0.0112 (Streeter and Chu, 1949); e) k/D = 0.0056 (Streeter and Chu, 1949); f) k/D = 0.0162 (Ambrose, 1954); g) k/D = 0.0337 (Ambrose, 1954). Here, k is the roughness height, and D is the diameter of the pipeline. The figure is from Perry et al. (1969).

The experimental results of Perry et al. (1969) showed distinguished turbulence behaviours between the different types of surface roughness. For the k-type roughness, the effective roughness height (k_s) was proportional to the dimension of surface roughness elements (k). For the d-type roughness, the effective roughness height was proportional to the thickness of the boundary layer δ or d, as illustrated in Figure 2.3.

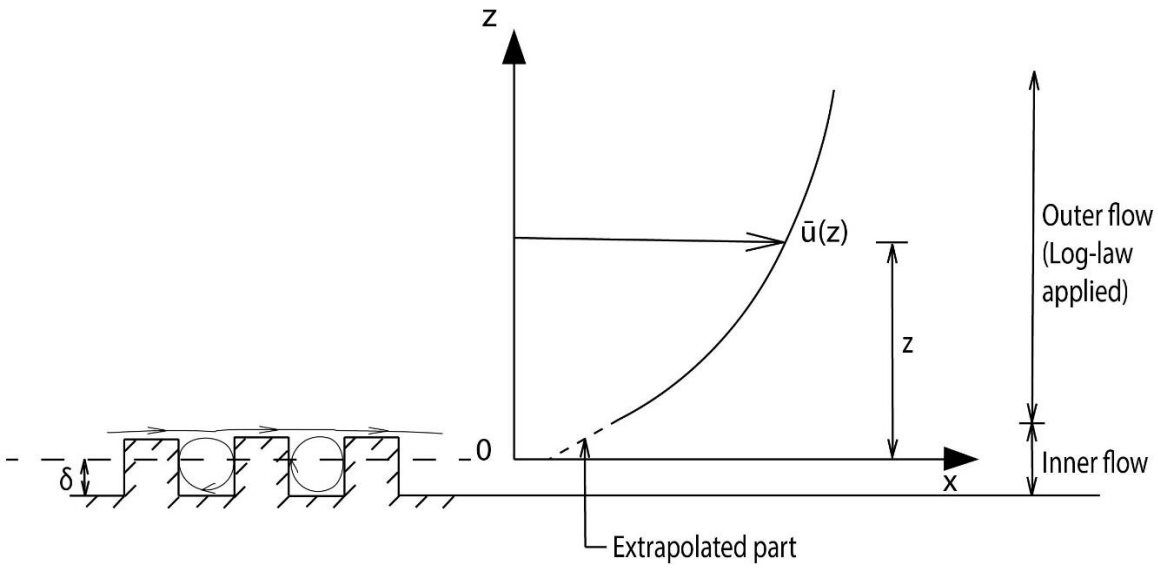

Figure 2.3 Turbulent boundary layer of flow over surface roughness (the d-type surface roughness), adapted from Perry et al. (1969).

Subsequent studies of the effects of roughness on turbulent flow introduced another type of surface roughness, called the intermediate type. The element spacing of this type of surface roughness is smaller than that of the k-type but larger than that of the d-type roughness. A number of researchers discussed the effects of these three types of surface roughness. Jiménez (2004) suggested L/h = 4~5 as the criterion for distinguishing the intermediate type of surface roughness from the d-type roughness and k-type roughness.

Agelinchaab and Tachie (2006) conducted experiments of turbulent open-channel flow over ribs of hemispheric shape. They used L/h = 2, 4, and 8 as the d-type, intermediate type, and k-type roughness. They observed different turbulence behaviours for the three types of surface roughness. In particular, the Reynolds stresses increased as L/h increased.

Coleman et al. (2007) used square ribs as roughness elements in their study of turbulent open-channel flow. They used several values for the spacing ratio L/h, varying from L/ h = 1 to 16 for the three types of surface roughness. They reported that for L/h = 5, the flow experienced a

transition from the d-type roughness and k-type roughness. Coleman et al. (2007) used double averaged methods to quantify the impact of surface roughness on turbulent flow. They observed increasing Reynolds stresses with increasing L/h. The maximum value of the Reynolds stress occurred at L/h = 8.

Manes et al. (2007) made measurements of shallow flow over the d-type roughness (with L/h = 1). They used spheres as roughness elements. They provided experimental evidence that shallow flow had no fully-developed log layer. However, the turbulent structure of the flow was similar to that of flow with a fully-developed log layer. Manes et al. (2007) suggested that the log-profile fitting method was invalid for shallow flows without a fully-developed log-layer. Note that the log-profile fitting method has been widely used for estimates of the shear velocity in turbulent flow in a wide range of fluid engineering applications.

Most recently, Singh et al. (2017) carried out an experimental study of turbulent flow over surface roughness. Their study used wood cubes as roughness elements. Their experiments involved three types of surface roughness, with L/h = 3, 5, and 9. The experiments produced measurements of near-bed velocities above and around the elements. These measurements were analysed using the double-averaged method. The results showed that for the three types of surface roughness, the velocity profile followed the logarithmic distribution above the cube top, and the linear distribution below the cube top. They also showed that the Reynolds stress increased with increasing L/h ratio.

In this thesis, we use roughness element spacing in consistence with previous research work. The ratios of L/h = 2, 4 and 6 represent the d-type, intermediate type, and k-type roughness, respectively.

2.2 Turbulent flow velocity

Open-channel flow is almost always turbulent. The instantaneous velocities of turbulent flow fluctuate around their mean values. Let (x, y, z) denote the Cartesian coordinates system. Let (u, v, w) denote the three instantaneous velocity components of turbulent flow in the x-, y-, and z-direction. The x-axis points in the streamwise direction, the y-axis points in the lateral direction across the channel, and the z-axis points upward in the vertical direction normal to the channel-bed. In Figure 2.4, instantaneous velocity components of turbulent flow are plotted as time series.

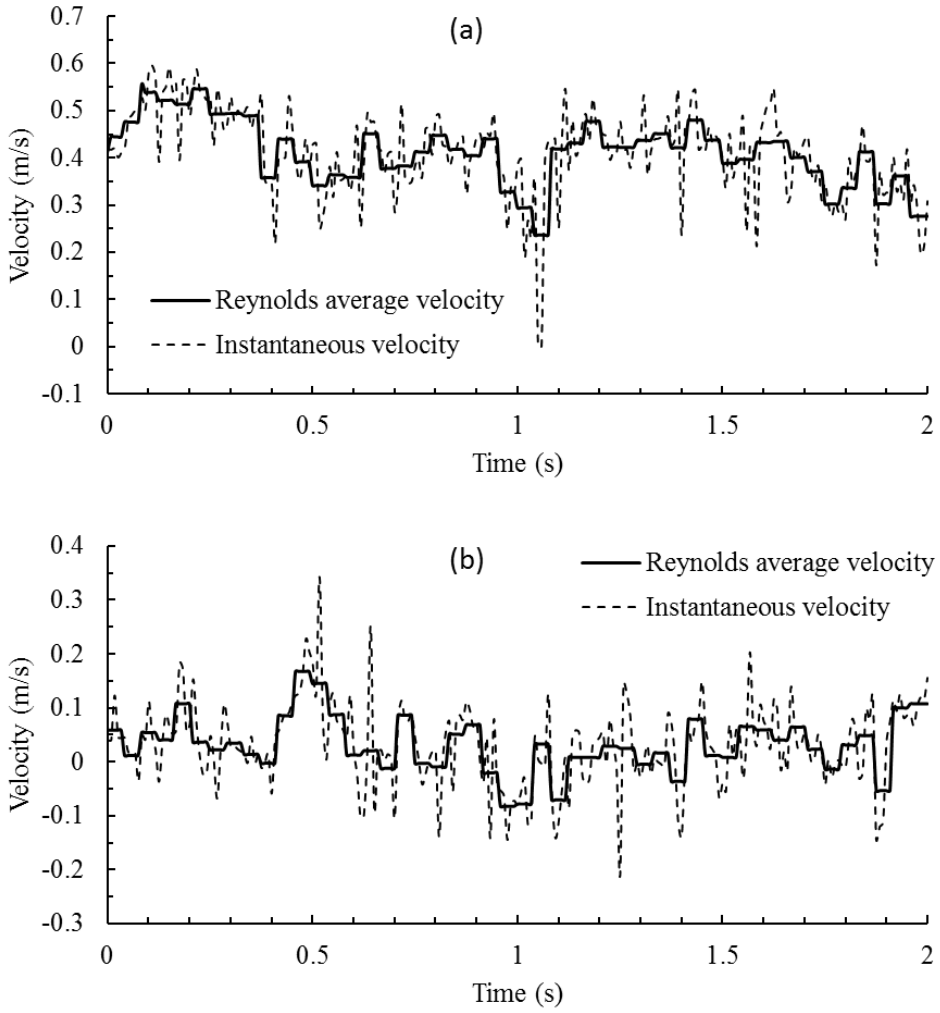

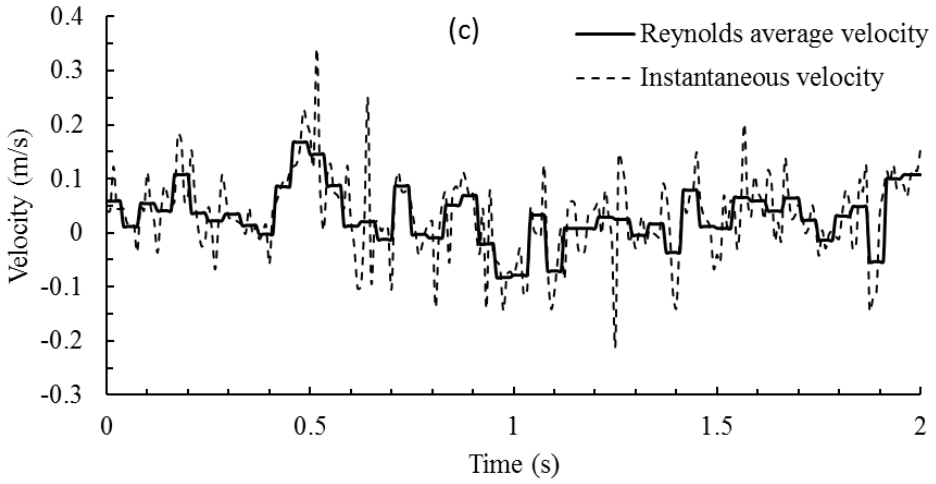

Figure 2.4 Time series of turbulent flow velocities from ADV measurements, showing instantaneous velocities with fluctuations around their values or Reynolds average velocities: (a) the longitudinal component; (b) the lateral component; (c) the vertical component.

On the basis of the Reynolds decomposition (Wilcox, 2006), the velocity components of turbulent flow can each be expressed as the sum of mean velocities ($\bar{u}$, $\bar{v}$, $\bar{w}$) and fluctuations (u', v', w'):

$$u = \bar{u} + u' \tag{2.1}$$

$$v = \bar{v} + v' \tag{2.2}$$

$$w = \bar{w} + w' \tag{2.3}$$

The time averages of fluctuations of individual velocity components are equal to zero

$$\overline{u'} = 0 \tag{2.4}$$

$$\overline{v'} = 0 \tag{2.5}$$

$$\overline{w'} = 0 \tag{2.6}$$

However, the time averages of the fluctuations between individual velocity components are generally not equal to zero

$$\overline{u'v'} \neq 0 \tag{2.7}$$

$$\overline{u'w'} \neq 0 \tag{2.8}$$

$$\overline{v'w'} \neq 0 \tag{2.9}$$

The three expressions given above physically represent the interactions between the velocity fluctuations in different directions.

2.3 Reynolds stresses

The specific Reynolds stresses are defined as

$$\tau_{xy} = -\overline{u'v'} \tag{2.10}$$

$$\tau_{xz} = -\overline{u'w'} \tag{2.11}$$

$$\tau_{yz} = -\overline{v'w'} \tag{2.12}$$

Schlitchting (1951, 9th edition, p. 503) explained the Reynolds stress as being due to the effect of fluctuating motion on the mean motion of turbulent flow. In Figure 2.5, such effect is illustrated for the near-bed region of turbulent flow. At the elevation of z = h, there is a small surface (dA) parallel tzo the bed. The small squares in the figure represent an element of fluid with density ρ. At z = h, $\bar{u}$ is the mean velocity in the *x*-direction, $\overline{w}$ is the mean velocity in the z-direction, u' is the velocity fluctuation of *u*, and w' is the velocity fluctuation of w.

For the small surface dA, the momentum of the flow in the *x*-direction is $(dA\rho wdt)u$, or $dA\rho uwdt$. From Equations (2.1) and (2.3), we obtain

$$uw = (\bar{u} + u')(\overline{w} + w') = \bar{u}\overline{w} + \bar{u}w' + \overline{w}u' + u'w' \tag{2.13}$$

Using Equations (2.4) and (2.6), the *x*-component of the momentum averaged over time (the average momentum flux) will be

$$dA\rho\overline{uw} = dA\rho(\bar{u}\overline{w} + \overline{u'w'}) \tag{2.14}$$

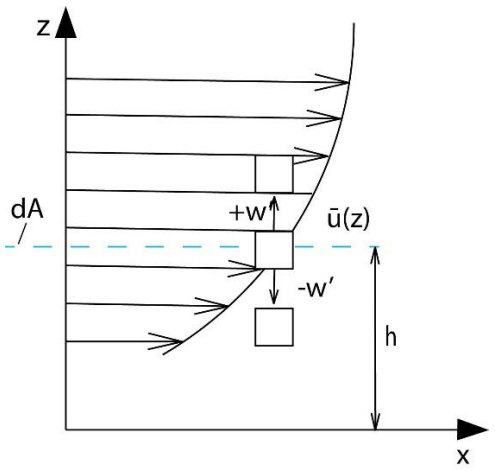

Figure 2.5 The average momentum flux in the x-direction (adopted from Schilichting 1951, 9th edition, p. 503)

which has the same dimension as force ($kg \cdot m/s^2$). One can see that the time averaged momentum flux is the sum of the mean motion ($\bar{u}\bar{w}$) and fluctuating motion ($\overline{u'w'}$). If the time-averaged momentum is divided by dA, the result will have the same dimension with stress (force per unit area), expressed as

$$\rho(\bar{u}\bar{w} + \overline{u'w'}) \tag{2.15}$$

The second term is the Reynolds stress, given by $-\rho\overline{u'w'}$.

2.4 Secondary flow

In an open-channel, turbulent flow has primary motion in the streamwise direction, with velocity *u*, as well as secondary motions in the lateral and vertical directions, with velocities *v* and *w*. It is often important to consider secondary motions. Strong secondary motions can lead to significant flow energy loss and increase channel resistance (Chow, 1959, p. 12). This thesis investigates the intensity of secondary motions, expressed as

$$U_s = \sqrt{\bar{v}^2 + \bar{w}^2}/\bar{u} \tag{2.16}$$

2.5 Vertical distribution of streamwise velocity

For a turbulent boundary layer next to the channel-bed, the shear stress τ is expressed as (Chow, 1951, p. 200)

$$\tau = \rho l^2 \left(\frac{d\bar{u}}{dz}\right)^2 \tag{2.17}$$

where l is a mixing length. Assume that l is proportional to the normal distance from the bed (or $l = \kappa z$), where κ is the von Kármán constant ($\kappa = 0.4$), and the shear stress is constant. We have

$$\frac{d\bar{u}}{dz} = \frac{1}{\kappa}\sqrt{\frac{\tau}{\rho}}\frac{1}{z} \tag{2.18}$$

Integrating Equation (2.18) vertically yields

$$\bar{u} = 2.5\sqrt{\frac{\tau}{\rho}}\ln\left(\frac{z}{z_0}\right) \tag{2.19}$$

where z_0 is the constant of integration.

At the bed, the friction velocity u_* is defined as $u_* = \sqrt{\frac{\tau_b}{\rho}}$. Thus, Equation (2.14) can be rewritten as

$$\frac{\bar{u}}{u_*} = 2.5\ln\left(\frac{z}{z_0}\right) \tag{2.20}$$

According to Nikuradse (1933), for a smooth bed, z_0 is proportional to the kinematic viscosity ν and friction velocity, in the form of $z_0 = \frac{m\nu}{u_*}$, where m is a constant equal to 1/9. For a rough bed, z_0 is proportional to the roughness height k, in the form of $z_0 = mk$, where m is a constant equal to 1/30. Therefore, Equation (2.20) becomes

$$\frac{\bar{u}}{u_*} = 2.5\ln\left(\frac{zu_*}{\nu}\right) + 5.1 \qquad \text{for smooth bed} \tag{2.21}$$

$$\frac{\bar{u}}{u_*} = 2.5 \ln\left(\frac{z}{k}\right) + 8.5 \qquad \text{for rough bed} \qquad (2.22)$$

These two equations describe the vertical distributions of the longitudinal velocity component in turbulent flow over a smooth bed and a rough bed, respectively. Both give a logarithmic distribution of the longitudinal velocity component. Logarithmic distributions have been widely used in numerical simulations of the turbulent flow.

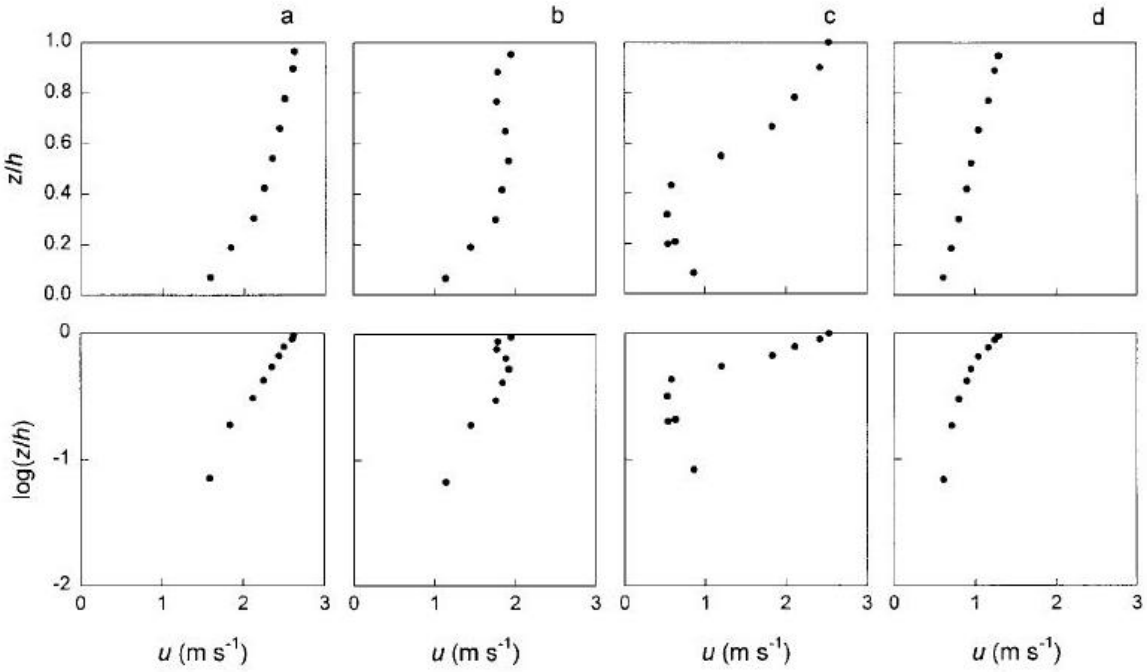

Figure 2.6 Four types of vertical distributions of mean longitudinal velocity in the horizontal: (a) approximately logarithmic profile; (b) S-shaped profile; (c) irregular profiles; (d) approximately linear profile (from Byrd et al., 2000).

However, field measurements indicated that the logarithmic distributions are not always adequate to describe flow conditions in rivers. Byrd et al. (2000) analysed velocity distributions using field measurements for rivers. They concluded that the logarithmic distributions only matched a small percentage (about 10%) of the field data. They suggested that besides the

logarithmic distribution, vertical distributions of the horizontal velocity components were of S-shape, irregularly shape, and linear shape, as shown in Figure 2.6. Wang et al. (2015) conducted experiments of turbulent flow in gravel-bed channels and observed S-shaped velocity distributions as well.

Chapter 3 Methodologies

3.1 Experimental setup

The experiments of turbulent flow were carried out in the Hydraulics Laboratory at Concordia University in a flume (Figure 3.1). The flume has vertical tempered-glass sidewalls and a flat stainless steel bed with zero slope. A section of the flume channel has a rough bed. Roughness was created by mounting roughness elements or cubes (Figure 3.2) on the otherwise flat bed. The experiment setup (Figure 3.1) consists of a channel of rectangular shape, a water supply reservoir, a pump, and an electromagnetic flowmeter. From upstream to downstream, the flume has a head section of 150 cm long, a main-channel section of 500 cm long, and a tail section of 150 cm long (Figure 3.3). Pipes connect the water tank and flume channel, forming a flow loop. The 500-cm main channel section has a width of 30.9 cm,

Acrylic cubes were arranged in rows and columns (Figure 3.2) with certain spacing (Figure 2.1) and mounted at three rectangular plates to create the d-type, intermediate type and k-type surface roughness. During an experiment, the cube-mounted plate in question was placed at the flume channel bed (Figure 3.1) with its ledge edge located at about 60 cm from the entrance of the channel (Figure 3.3). During an experiment, water from the reservoir flows (by pumping) through the head section, main channel section, and tail section, and returns to the reservoir. The head section has curved sidewalls (Figures 3.3). The curved sidewalls cause flow streamlines to contract in the horizontal plane, and thus help create uniform approach flow to the main channel section. In addition to sidewall curvature, this head section has a plate that floats at the water surface for damping turbulence in the approach flow. The tail section has an adjustable gate for the control of flow depth in the main channel section with cubes mounted at the bed.

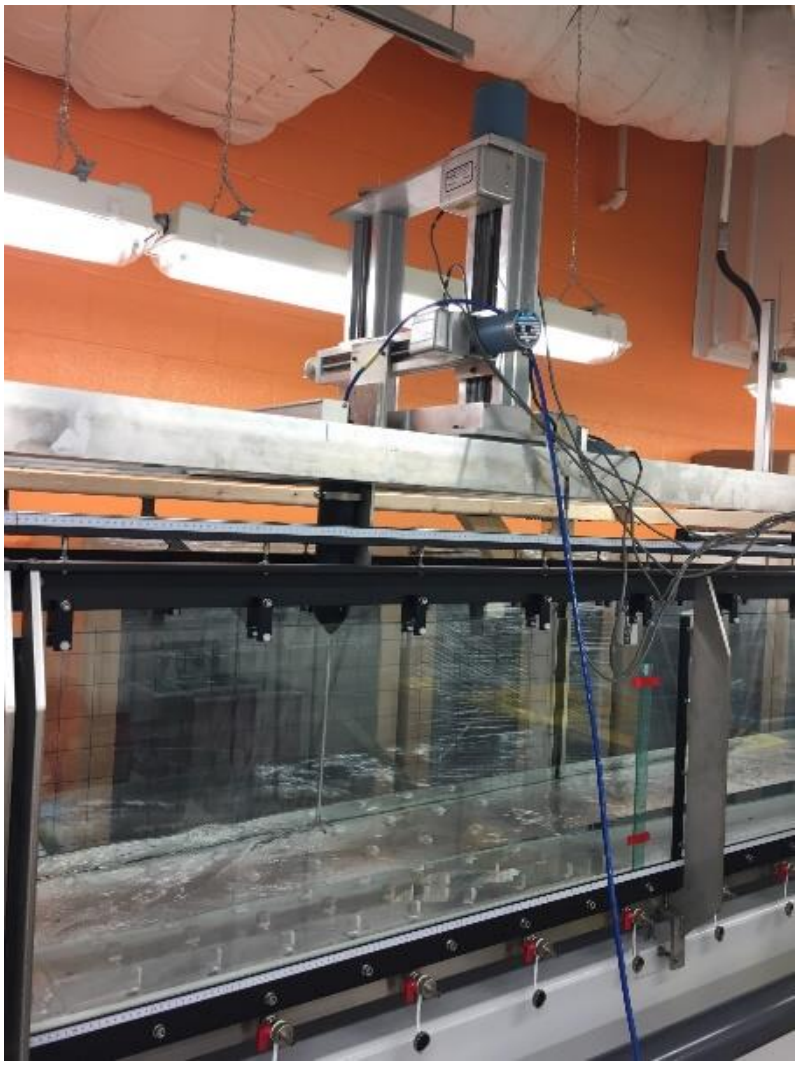

Figure 3.1 Experimental setup: a photo of the flume channel, showing an array of acrylic cubes mounted at the channel-bed, a step motor installed above the channel, and an acoustic Doppler velocimeters (ADV) mounted on the step motor.

(a)

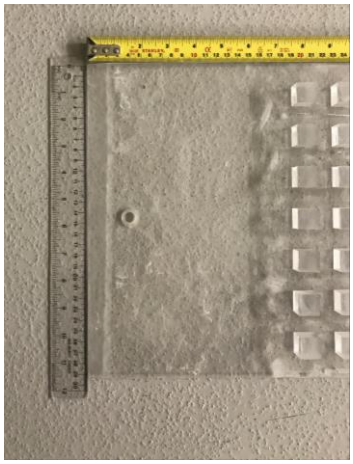

(b)

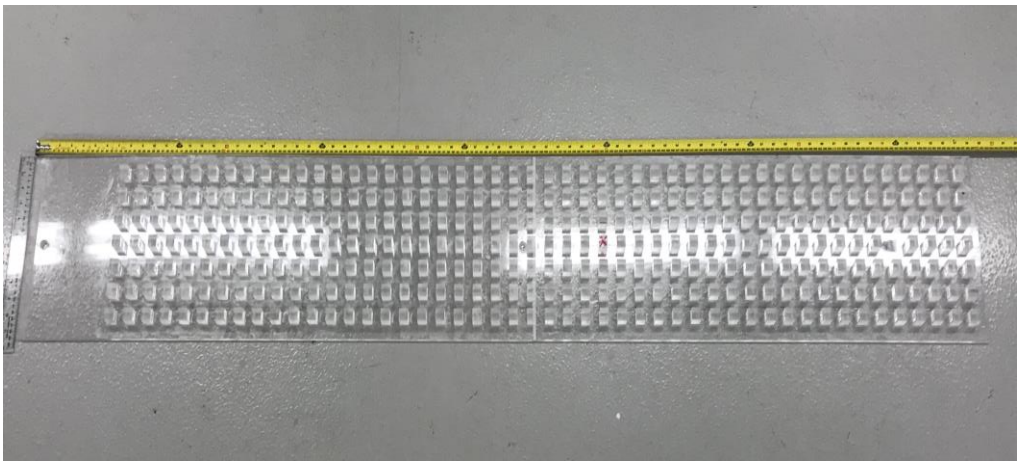

Figure 3.2 Photo of a bottom plate with cubes mounted to create the d-type roughness: (a) close up view of the upstream edge (or leading edge) of the plate; (a) plan view of the plate.

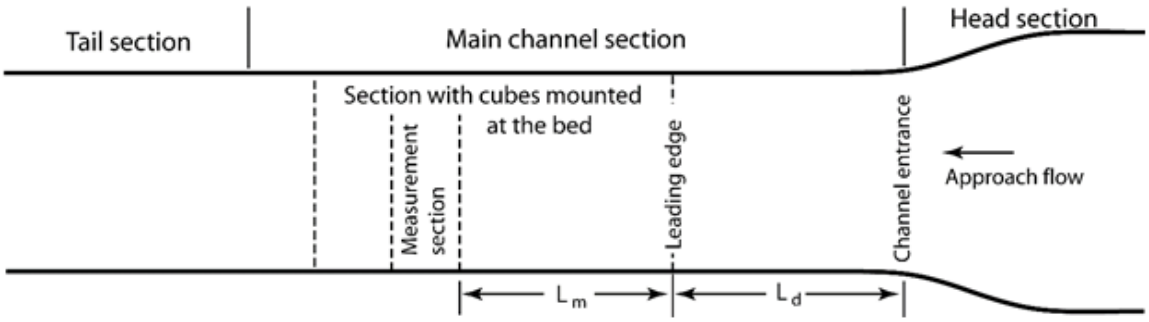

Figure 3.3 Plan view of the flow channel.

3.2 Roughness surface

Acrylic cubes as roughness elements were affixed to acrylic sheets (Figure 3.2) that were mounted to flume channel-bed (Figure 3.1). The length of each side of the cubes is 19.02 mm (or 3/4 inches). The acrylic sheets plates have a length of 1980 mm, a width of 309 mm, and a thickness of 6.35 mm (or 1/2 inches). To an observer facing downstream, the first row of the cubes were affixed at a distance of 19 cm from the upstream edge of the acrylic sheets.

The cube-mounted acrylic sheet as a d-type roughness surface has seven cubes on each row at uniform spacing. The spacing ratio (Figure 2.1) is L/h = 2, meaning that the distance between two consecutive cubes is 19.02 mm. The cube-mounted sheet as an intermediate roughness surface has three cubes on each row at uniform spacing. The spacing ratio (Figure 2.1) is L/h = 4. In other words, the distance between two consecutive cubes is 57.06 mm. The cube-mounted sheet as a k-type roughness surface has three cubes on each row. The spacing ratio is L/h = 6, meaning that the distance between two consecutive cubes is 95.01 mm.

3.3 Positions of flow velocity measurements

An array of positions in the flow over roughness elements (Figures 3.1 and 3.2) were selected for point measurements of flow velocities in three orthogonal directions. For the d-type surface roughness (L/h = 2), the measurement positons in a channel cross section are shown in Figure 3.4. The surface of the acrylic sheets at which cubes (roughness elements) were affixed is taken as the vertical datum (z = 0). In the vertical direction, the z coordinates (Table 3.1) of the measurement positions measure the vertical distance of ADV's remote sampling volume upward from the datum. It is understood that the remote sampling volume is located 5 cm below from the tip of the ADV transmitter.

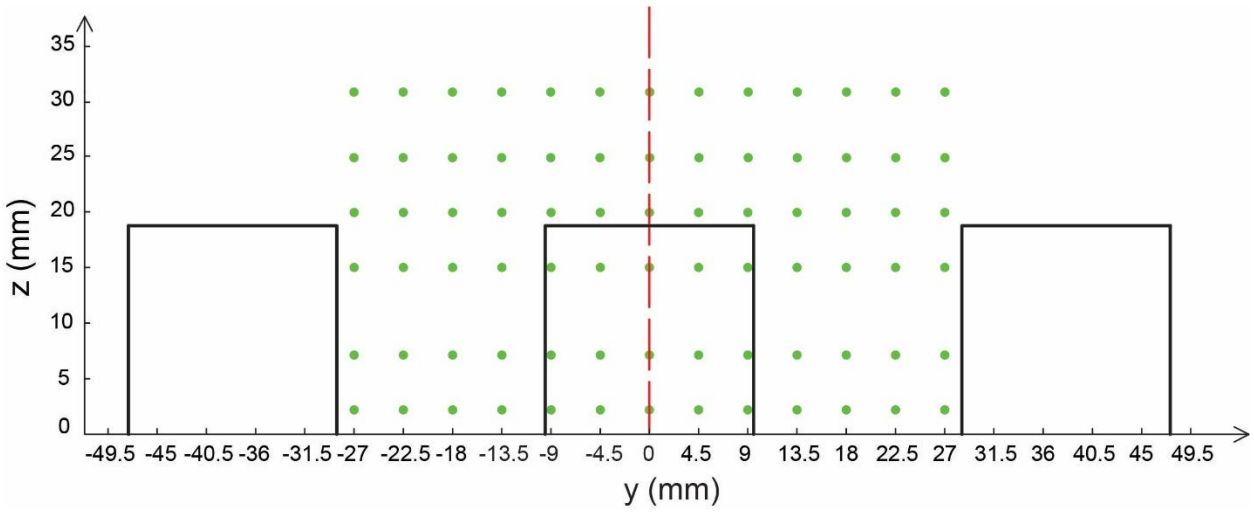

Figure 3.4 A vertical cross-section across the channel width, showing the measurement positions (green circles) for the d-type surface roughness. The dashed red line marks the longitudinal centre (y = 0) of the flume channel. The direction of the primary flow is directly out of the page.

Table 3.1 Vertical positions from which ADV measurements of flow over the d-type, intermediate type, and k-type of roughness surfaces were made. The roughness height is h = 19.02 mm. The depth of flow is H = 88, 90, and 90 mm for the experiments of flow over the three types of roughness surfaces, respectively.

d-type roughness			Intermediate type roughness			k-type roughness		
z (cm)	z/h	z/H	z (cm)	z/h	z/H	z (cm)	z/h	z/H
31	1.630	0.352	30	1.577	0.333	31	1.630	0.344
25	1.314	0.284	25	1.314	0.278	25	1.314	0.278
20	1.052	0.227	19	0.999	0.211	19	0.999	0.211
15	0.789	0.170	14	0.736	0.156	15	0.789	0.167
7	0.368	0.080	7	0.368	0.078	7	0.368	0.078
2	0.105	0.023	2	0.105	0.022	2	0.105	0.022

In fact, ADV measurements of flow velocities from the positions shown in Figure 3.4 produce 13 vertical profiles of velocity components. The lateral positions (Table 3.2) of these profiles are symmetrical about the longitudinal centre (y = 0) of the flume channel. Between two adjacent profiles, the lateral spacing is $\Delta y = 4.5$ mm. Thus spacing gives fine resolutions, in the cross-channel direction, of the flow structures. Each profile consists of measurements at six elevations (Table 3.1), three of which are within the cavity ($z/h < 1$) between adjacent roughness elements, one matches the top of the elements ($z/h \approx 1$), and two are above the top but within two times the roughness height ($1 < z/h < 2$). Thus, the measurements are considered as near-bed measurements.

For the experiment involving the d-type roughness, there were a total of 11 vertical cross sections (like the one shown in Figure 3.4) from which ADV measurements were made; these vertical cross sections were evenly spaced in the along-channel direction (Figure 3.5). The spacing is $\Delta x = 5.7$ mm, which gives fine resolutions of the flow structures in the along-channel direction. The most upstream vertical cross section is located x = -11.4 mm, whereas the most downstream vertical cross section is located at x = 45.6 mm.

Table 3.2 Lateral positions of ADV profiles for the experiments involving the d-type, intermediate type, and k-type of roughness surfaces. Note that y = 0 at the longitudinal centre of the channel, and the longitudinal centres of the row of cubes along the longitudinal centreline of the channel.

Roughness type	y (mm)
d-type	-27.0, ……, -9.0, -4.5, 0, 4.5, 9.0, ……, 27.0
Intermediate type	-31.5, ……, -9.0, -4.5, 0, 4.5, 9.0, ……, 31.5
k-type	-36.0, ……, -9.0, -4.5, 0, 4.5, 9.0, ……, 36.0

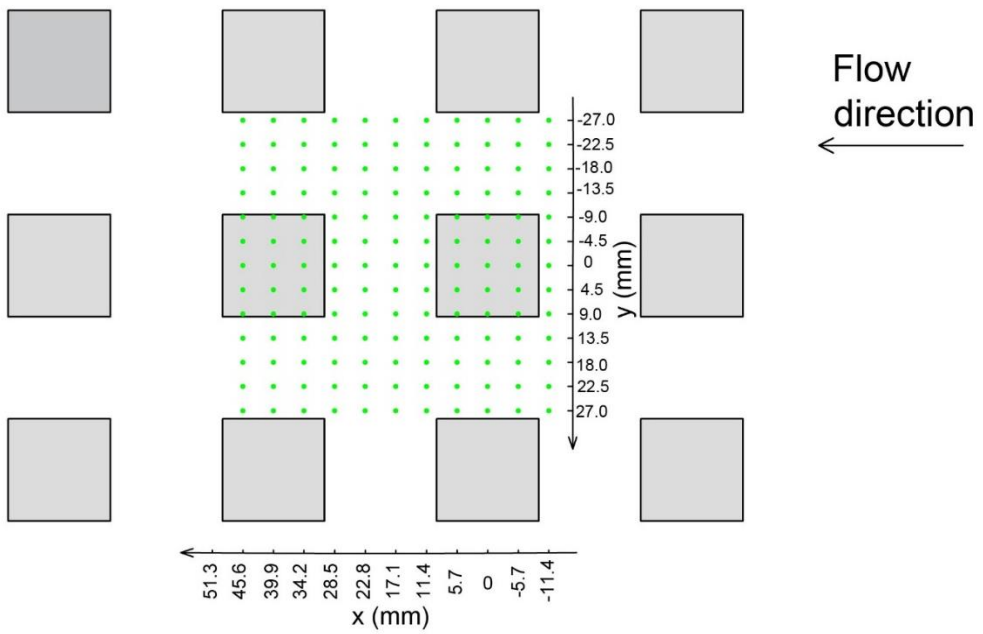

Figure 3.5 Plan view of 11 cross sections for ADV measurements from d-type roughness experiments.

For the k-type roughness experiments, there were a total of 24 vertical cross sections from which ADV measurements were made. Each of them crossed the channel width. These vertical cross sections were evenly spaced in the longitudinal direction (Figure 3.6). The spacing is Δx = 5.7 mm. The most upstream cross section is located x = 34.2 mm, whereas the most downstream cross section is located at x = -96.9 mm. Measurements from each of the cross sections produce 17 vertical profiles of velocity components. Their lateral positions (Table 3.2) are symmetrical about the longitudinal centre (y = 0) of the channel. The lateral spacing between two adjacent profiles is Δy = 4.5 mm. Like the case of the d-type roughness, each profile consists of measurements at six elevations (Table 3.1): three within the cavity between adjacent roughness elements, one at the top of the elements, and two above the top but within two times the roughness height.

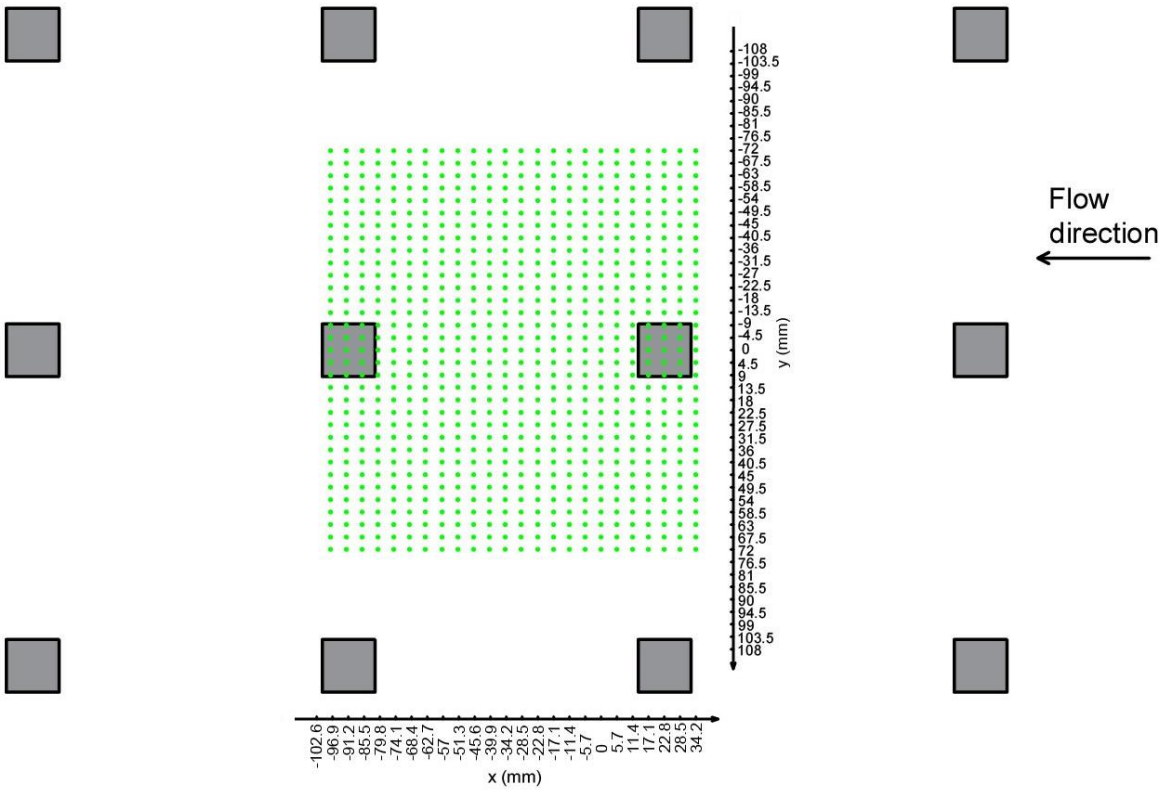

Figure 3.6 Plan view of 24 cross sections for ADV measurements from experiments involving the k-type roughness.

For the experiment involving the intermediate-type roughness, there were a total of 18 vertical cross sections for ADV measurements. These cross sections each crossed the channel width. They were evenly spaced in the along-channel direction (Figure 3.7), at a spacing $\Delta x = 5.7$ mm. The most upstream vertical cross section is located x = -11.4 mm, whereas the most downstream vertical cross section is located at x = 85.5 mm. Measurements from each of the 18 cross sections produce 15 vertical profiles of velocity components. The profiles' lateral positions (Table 3.2) are symmetrical about the longitudinal centre (y = 0) of the flume channel. The lateral spacing between two adjacent profiles is $\Delta y = 4.5$ mm. Like the cases of the d-type and k-type roughness, each of the profile consists of measurements at six elevations (Table 3.1): three within the cavity between adjacent roughness elements, one at the top of the elements, and two above the top but within two times the roughness height.

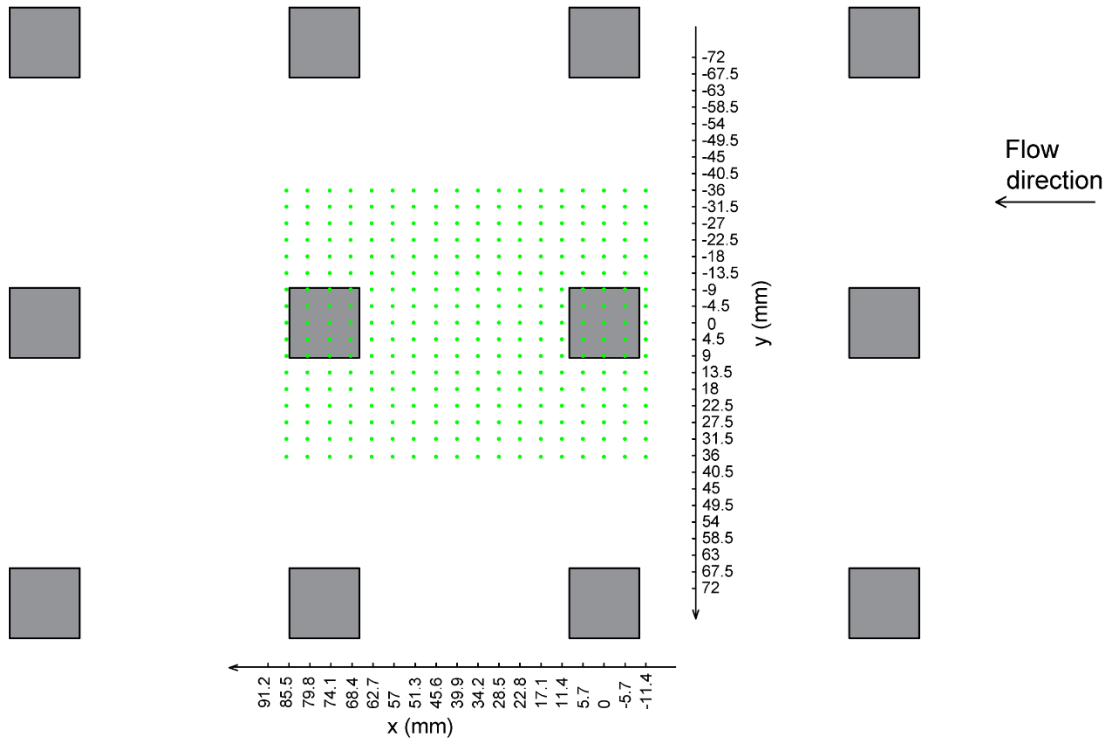

Figure 3.7 Plan view of 18 cross sections for ADV measurements from experiments involving the intermediate-type roughness.

For all the three types of surface roughness, the measurements cover the space between two consecutive cubes in the along-channel direction (from the upstream face of the cube at upstream to the downstream face of the cube at downstream), including the cavity between the two cubes. It is understood that those profiles directly above the top of a cube contain no velocity measurements at elevations below the top (Figure 3.4), because the ADV sampling volume would be located inside the solid cube. The no measurement region is bounded by -12 mm $\leq y \leq$ 12 mm and $0 \leq z \leq$ 20 mm for the three types of surface roughness.

3.4 ADV setup

A Nortek Vectrino+ acoustic Doppler velocimeter (ADV) was used for velocity measurements from the experiments involving the three types of surface roughness. The ADV recorded instantaneous velocity components at a single-point with with a maximum frequency of 200 Hz. We made several tests of the ADV probe to determine the best configurations for the ADV by using the Probe Check function. We followed the guidelines of the comprehensive manual of ADV from the manufactory. A screenshot of the test results is shown in Figure 3.8 and the configuration is presented in Figure 3.9.

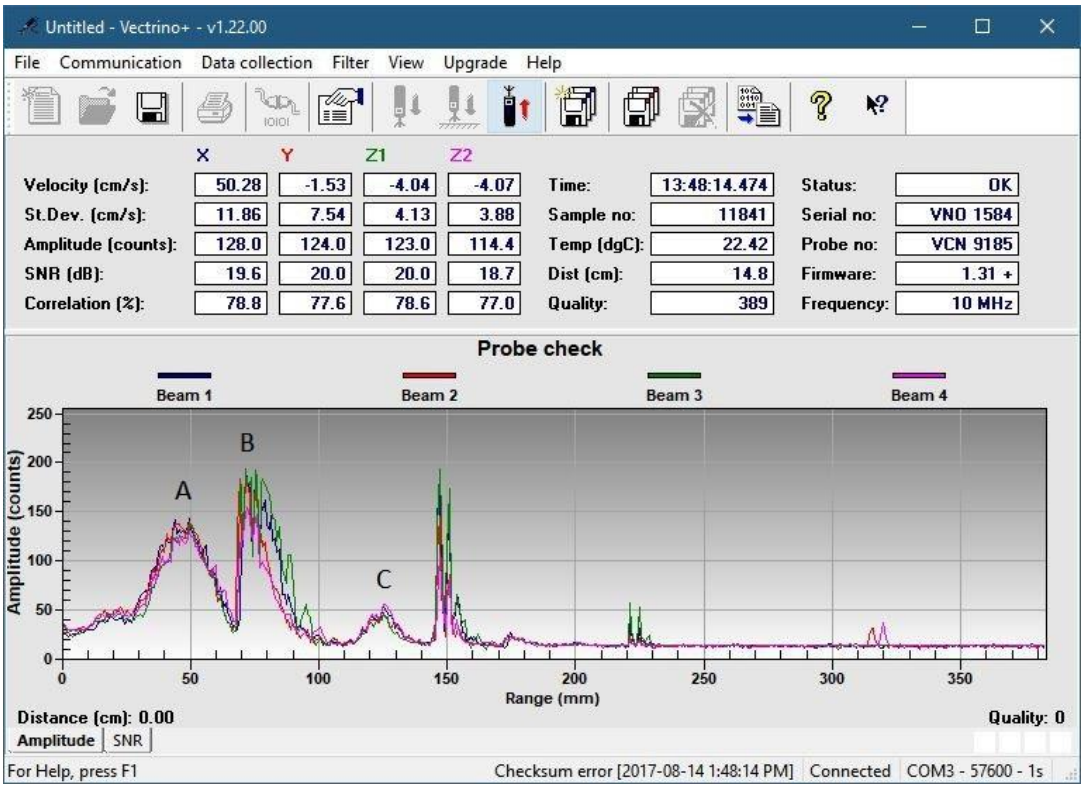

Figure 3.8 A screenshot of the Probe Check for the ADV probe used in this experimental study.

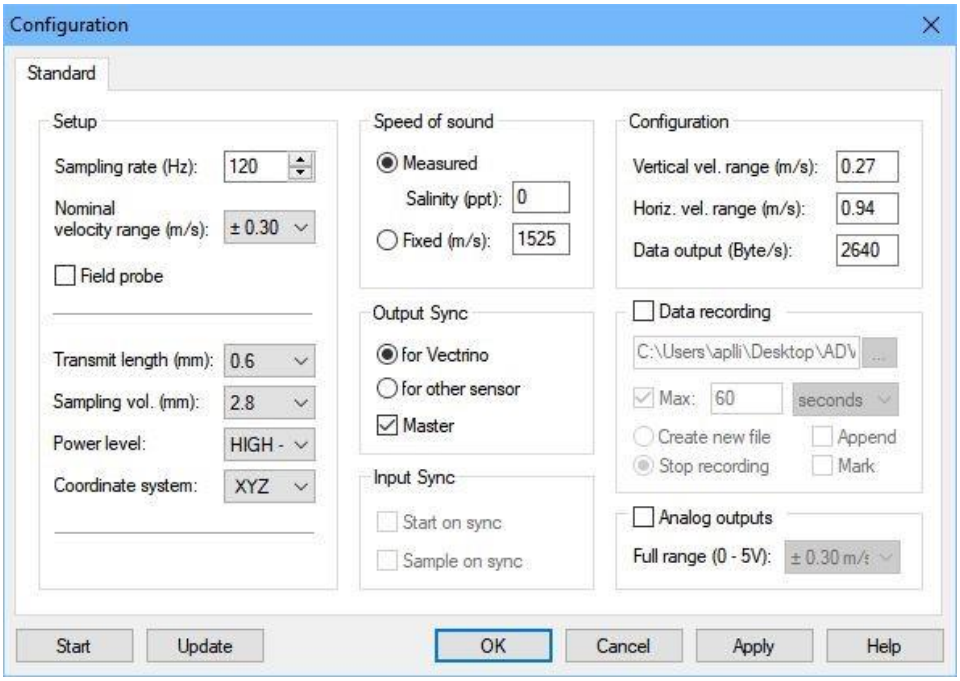

Figure 3.9 A screenshot of the configurations for the ADV used in this experimental research.

In Figure 3.8, the four coloured graphs (blue, red, green and pink) represent the four beams collected by the corresponded probes. There are three important peaks: peak A is the transmit pulse, peak B is the area around the measuring volume (2.8 mm) and peak C is the boundary echo (about 13 mm from the boundary). Additional peaks in the figure are reflections. It should be mentioned that for this test, the constant signal level (the noise floor) is around 10 – 20 counts (lower than 60 counts), which indicates there are not enough scatters in the water. Therefore, for subsequent experiments, we added seeding materials into the water to ensure a signal level of 60 counts for all the formal experiments.

Figure 3.9 shows configurations for all the experiments. There are three important parameters: sampling rate, velocity range. For all the experiments, sampling rate is set to 120 Hz (200 Hz is the maximum value), so that there are 7,200 collects for each velocity component (u, v

and *w*) in one minute. Nominal velocity range is related to pulse interference (weak spots). According to the comprehensive manual of ADV (pp. 92), for the nominal velocity range of 0.3 m/s, the distances to the boundary (the bed) where weak spots occur are 38 mm and 75 mm. In our experiments the measuring elevations are 7, 12, 19, 20, 24, 25, 30, 35 and 36 mm, respectively. Thus, the nomination of 0.3 m/s is suitable for our experiments. The sampling volume is another important parameter for ADV. The sampling volume is a cylinder located 50 mm below the transmitter. In Figure 3.9, the "Transmit length (mm)" is the height of cylinder which is set to 0.6 mm for all the experiments. The "Sampling vol. (mm)" is the diameter of the sampling volume which is set to 2.8 mm for all the experiments. It should be mentioned that the lowest measuring point in our experiment is 7 cm above the bed, meaning that there is a distance of 20 mm between the bed and the upper surface of the cylinder and the height of 0.6 mm ensures the sampling volume does not extend into the bed.

A review of the literature shows that in most studies where ADV measurements were involved, ADV probes are commonly kept at an intended position for three minutes, recording instantaneous velocity components (*u*, *v*, *w*) at a single-point. In the Hydraulics Laboratory at Concordia University, we performed some flow experiments in the flume (Figure 3.1), and recorded instantaneous velocity components at a sampling rate of 120 Hz for three minutes. This produces 21600 records at a single-point. We determined the Reynolds averaged flow velocities as

$$\bar{u} = \frac{\sum_{i=1}^{N} u_i}{N} \tag{3.1}$$

$$\bar{v} = \frac{\sum_{i=1}^{N} v_i}{N} \tag{3.2}$$

$$\bar{w} = \frac{\sum_{i=1}^{N} w_i}{N} \tag{3.3}$$

where N = 21600. From the experiment, we recorded instantaneous velocity components at a sampling rate of 120 Hz for one minute, and obtained 7200 records at a single-point. We compared the Reynolds averaged flow velocities between the three minutes and one minute records at more 30 selected measurement positions, and obtained the same statistical results. Therefore, one minute records are sufficient for this study. A reduction in ADV recording from three to one minute has improved the efficiency of data collection from the experiments. The results presented in Chapter Four of this thesis are based on one-minute ADV records at individual points.

3.5 Positioning of ADV probe

A step motor was used to accurately position the ADV probe for measurements of instantaneous velocity components at intended points. The ADV probe was affixed to the step motor mounted on a pair of aluminium railings on the top of the flume channel (Figure 3.1). The step motor has three movable axes in the along-channel, cross-channel and vertical directions. In each of the directions, the movements were computer-controlled by specified distance steps. The accuracy was as 0.1 mm. Once the probe reached the specified (x, y, z) coordinates, its position was locked for ADV recording.

3.6 Processing of ADV data

Raw data of velocity collected by the ADV probe were imported into the velocity signal analyser, VSA (Version 1.5.62). Jesson et al. (2015) successfully applied the VSA to process a large volume of velocity data in their study. We followed Jesson et al.'s (2015) procedures and obtained filtered velocity components (u, v, w). The procedures involve the use of the phase-space thresholding

method to de-spike the raw data. Goring and Nikora (2002) firstly introduced this method and claimed that it has better performance than other dis-piking methods. Thus, we chose phase-space thresholding method for this study. The filtered velocity data were imported into MATLAB (R2016a) for further calculations.

3.7 Hydraulic conditions of the experiments

A summary of the hydraulic conditions of the experiments is given in Table 3.3. The three experiments used the d-type, intermediate type, and k-type roughness, respectively. The discharges were set to about Q = 14.72 L/s for the d-type experiment, 14.76 L/s for the intermediate type experiment, and 14.46 L/s for the k-type experiment. The discharge was measured in the pipe downstream of the pump, using an electromagnetic flowmeter. The depths of flow were 8.8 cm for the d-type experiment, and 9 cm for the other two types of roughness experiments. The Reynolds numbers were $Re = UR/\nu > 28{,}000$ for all the three cases, where U is the cross-sectionally averaged velocity of the approach flow, R is the hydraulic radius, and ν is the kinematic viscosity of water. These high values of Re ensured that the flow was turbulent.

Table 3.3 Hydraulic conditions of the experiments of flow over roughness elements. M represents the number of velocity profiles made from of the experiments.

Experiment	L/h	Q	H	U	Re	L_e	M
		(L/s)	(cm)	(cm/s)		(m)	
d-type	2	14.72	8.8	54.1	29,095	1.42	143
Intermediate-type	4	14.76	9	53.1	28,932	1.41	306
k-type	6	14.46	9	52.0	28,344	1.40	792

In Table 3.3, the entrance length, L_e, for the turbulent flow was estimated using the method of Çengel and Cimbala (2004, p. 327)

$$L_e = 1.359 D R_{e_D}^{1/4} \tag{3.4}$$

where D is the diameter of the tube. In this study, we replaced D by the depth of flow. Some researchers have suggested that the entrance length can be approximated as

$$L_e \approx 10D \tag{3.5}$$

For the experimental conditions listed in Table 3.3, Equation (3.4) gives a maximum value of 1.42 m for L_e, whereas Equation (3.5) gives a maximum value of 0.99 for Le. As pointed out in Section 3.2, the most upstream row of cubes in our experiments were located at a distance of about 19 cm from the upstream edge of the acrylic sheets at which the cubes affixed (Figures 3.1 to 3.3) and all the measurements were made at about 1.65 m from the upstream edge. Thus, there was a distance of 1.46 m for the flow to develop over the cubes. This distance is sufficient for the flow to develop into fully turbulent conditions before reaching the measurement section in our experiments. The experimental results are presented and discussed in the next chapter.

Chapter 4 Results and Discussions

4.1 Primary flow

The Reynolds average velocity component, $\bar{u}$, (Equation 3.1) in the longitudinal direction describes the primary flow. Note that $\bar{u}$ is in the horizontal direction. Vertical profiles of $\bar{u}$ reveal how $\bar{u}$ varies with vertical distance, z, from the bed toward the water surface (Figure 3.4). A total of 143, 306, and 792 profiles were obtained from the experiments of turbulent flow over the d-type, intermediate type, and k-type roughness surfaces, respectively. Examinations of these profiles have led to the identification of six distinct profile shapes, named as Type 1 throughout Type 6. The criteria for identification are such that at the basic level, we distinguish between linear and nonlinear variations of $\bar{u}$. At the next level, we determine whether the shapes of profiles are a combination of linear and nonlinear variations over the water column. We provide examples of types 1 to 6 of profiles below. The normalized vertical distance (z/h) by the roughness height can be found in Table 3.1, ranging from 0.105 to 1.630.

4.1.1 Type 1 profiles of longitudinal velocity

An example of Type 1 profiles is depicted in Figure 4.1. This example profile was observed from the experiment that involved the k-type roughness (Figure 3.6). The main feature of this profile is combined linear and nonlinear variations between the bed and water surface. Specifically, the three data points in the upper water column follow a straight line, whereas the other three data points in the lower water column show a nonlinear trend. The straight line is seen to extend further downward to the elevation of the top of the cubes. Note that $\bar{u}$ increases suddenly at the second lowest elevation above the channel bed. Such sudden changes are velocity overshooting. Note that

$\bar{u}$ has a magnitude of 29.3 cm/s at z = 2 mm and reaches a magnitude of 52.4 m/s at z = 31 mm. This is in comparison to the approach flow velocity of U = 52 cm/s (Table 3.3).

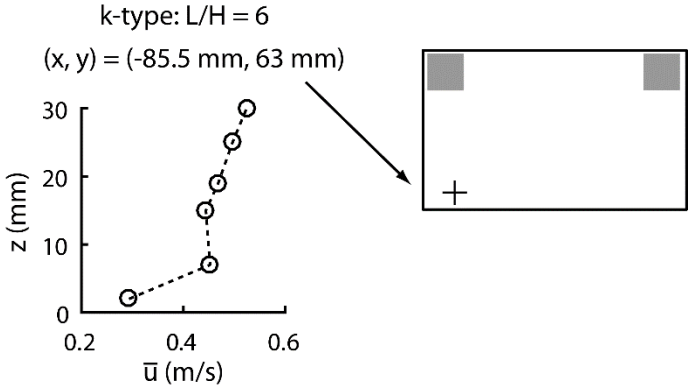

Figure 4.1 Vertical profile of $\bar{u}$ observed from the k-type roughness experiment. The horizontal location of the observations is marked as the plus symbol '+' in the insert panel, where the approach flow is from right to left.

4.1.2 Type 2 profiles of longitudinal velocity

For Type 2 profiles, two examples are shown in Figures 4.2a–b. The distinct shape of these profiles shows nonlinear variations in $\bar{u}$ with z in the entire water column. Clearly, $\bar{u}$ has a minimum value immediately above the channel-bed and a maximum value close to the water surface. There is no velocity overshooting in this case. Type 2 profiles can further be divided into two sub-types: One shows strong nonlinearity in the cavity of cubes. The other shows relatively weak nonlinearity there. The shape of Type 2 profiles in the cavity of cubes is similar to that of Type 1 profiles shown in Figure 4.1.

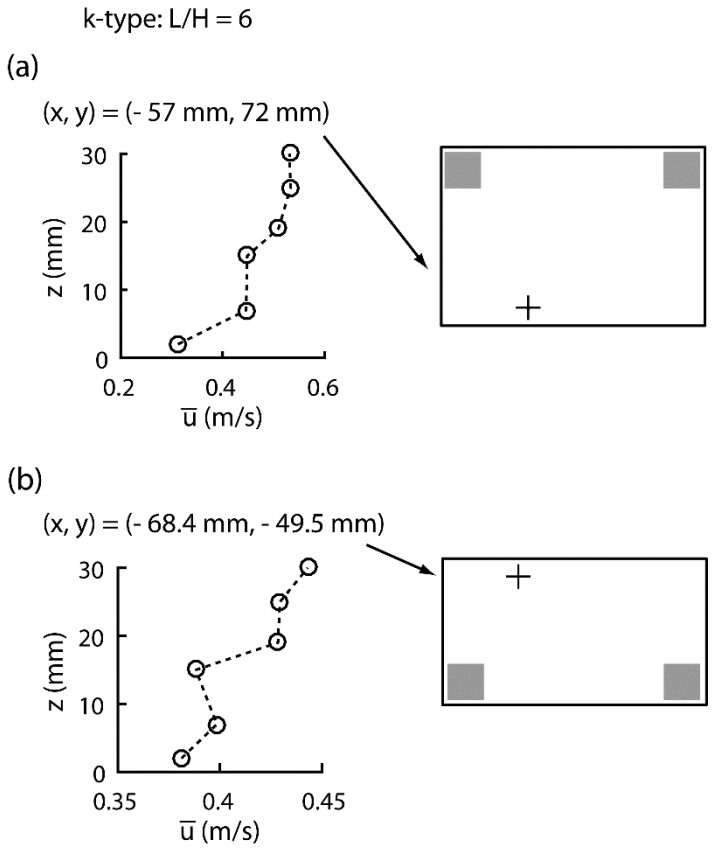

Figure 4.2 Vertical profiles of $\bar{u}$ observed from the k-type experiments. The horizontal locations of the observations are marked as: (a) the plus symbol '+', and (b) the cross symbol '×' in the insert panel, where the approach flow is from right to left.

4.1.3 Type 3 profiles of longitudinal velocity

For Type 3 profiles, three examples of are plotted in Figures 4.3a-c. This type of $\bar{u}$ profiles shows a linear distribution combined with a nonlinear distributions. The linear distribution appears at the relatively higher elevations. The nonlinear distribution appears at the relatively lower elevations with the relatively large velocity at the second lowest elevation. In terms of the slope of the linear portion of $\bar{u}$ with respect to z above the top of cubes, Type 3 profiles can further be divided into three subtypes: the slope progressively increases from Figure 4.3a to Figure 4.3b to Figure 4.3c. The three profiles shown were observed from the k-type roughness experiment (Figure 3.6).

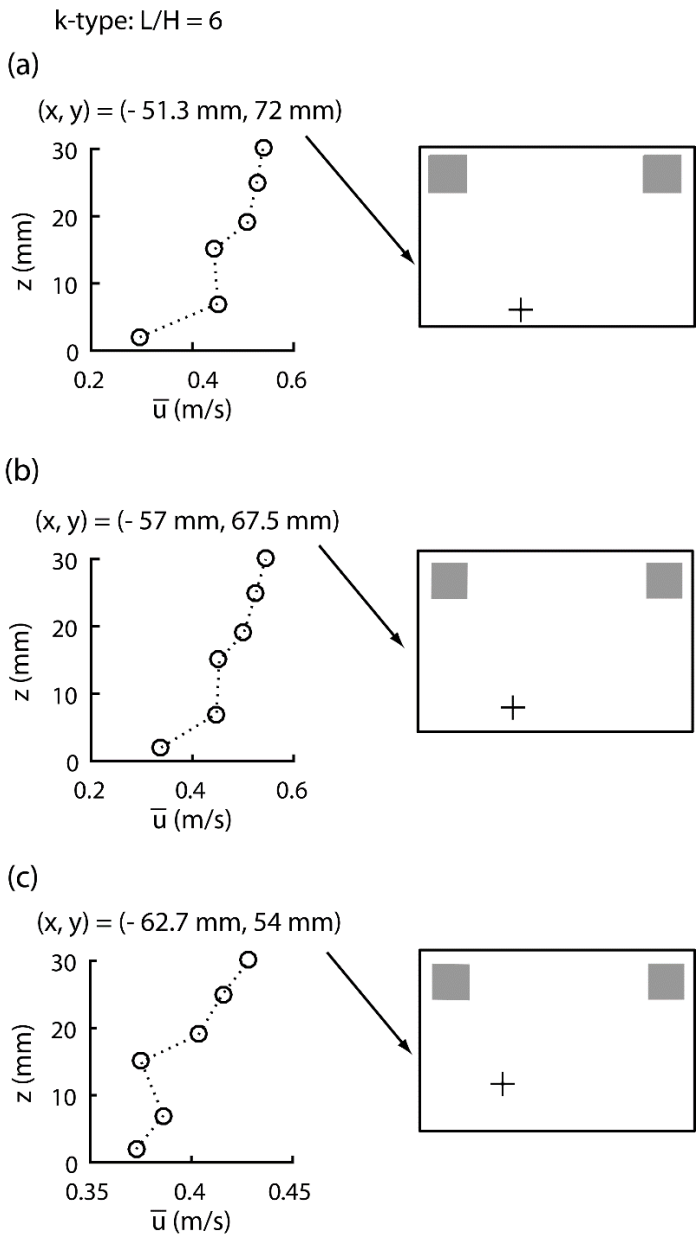

Figure 4.3 Vertical profiles of $\bar{u}$ observed from the k-type experiments. The horizontal locations of the observations are marked as: (a) the plus symbol '+', (b) the cross symbol '×', and (c) the open circle 'o' in the insert panel, where the approach flow is from right to left.

4.1.4 Type 4 profiles of longitudinal velocity

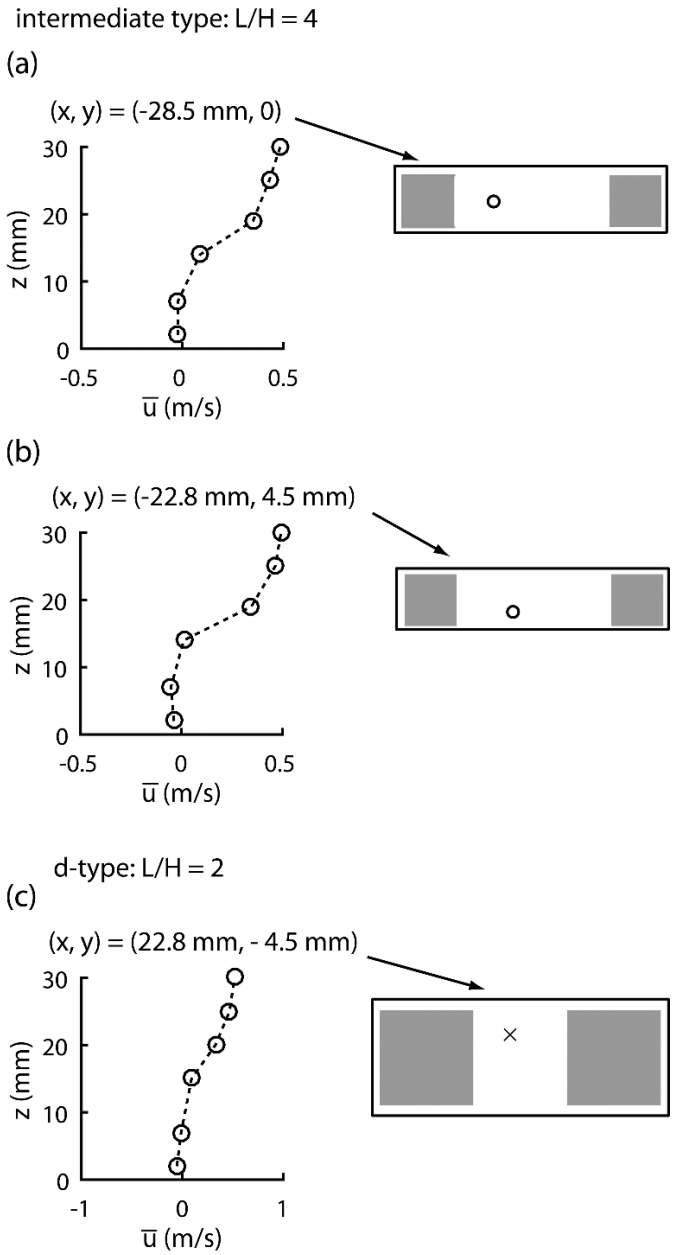

Figure 4.4 Vertical profiles of $\bar{u}$ observed from the intermediate-type experiments. The horizontal locations of the observations are marked as: (a) the plus symbol '+', and (b) the cross symbol '×', where the approach flow is from right to left.

For Type 4 profiles, three examples are shown in Figures 4.4a-c. The most significant feature of these profiles is flow separation at the channel-bed. The bed shear stress vanishes or is negligibly small. Above the top of cubes, the profile shape appears to follow a logarithmic distribution.

4.1.5 Type 5 profiles of longitudinal velocity

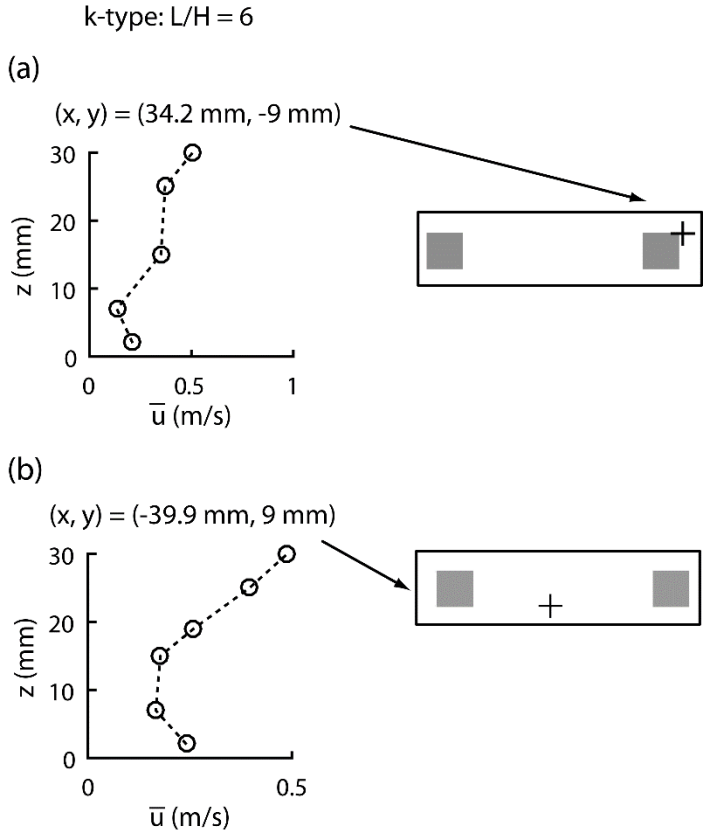

Figure 4.5 Vertical profiles of $\bar{u}$ observed from the k-type experiments. The horizontal locations of the observations are marked as: (a) the plus symbol '+', and (b) the cross symbol '+', where the approach flow is from right to left.

For Type 5 profiles, two examples are plotted in Figures 4.5a-b. Type 5 profiles distinguish from the four types of profiles discussed earlier in that this type profiles have the minimum velocity at the second lowest elevation (z = 7 mm), as opposed to at the lowest elevation. In Figure 4.5a, the velocity increases slightly toward the water surface. In Figure 4.5b, the distribution is linear at the four elevations of z = 15, 19, 25 and 31 mm, which is different from the profile shape shown in Figure 4.4b, and the velocity increases toward the water surface.

4.1.6 Type 6 profiles of longitudinal velocity

For Type 6 profiles, four examples are plotted in Figures 4.6a-d. The main feature of the profiles is linear or quasilinear distributions. The velocity increases monotonously with vertical distance from the bed toward the water surface. Such profiles were observed from all the three types of roughness experiments. In Figures 4.6a and 4.6c, the upper three data points as well as the lower three data points are co-linear, and the portion of the profiles in the cavity of cubes has a slope that slightly smaller than the portion above the top of cubes. In Figure 4.6b, the all data points fit essentially into a straight line. In Figure 4.6d, the profile shows small departure (wavy pattern) from a straight line. If we connect the highest and lowest data points with a straight line, the data point at the second highest elevation is above this line.

We conclude that a variety of mean velocity profiles were obtained from the experiments involving the three types of roughness surfaces. In general, velocity variations with distance from the bed to water surface are an increase in velocity. In most of the cases, the minimum velocity occurs at the lowest elevation, and the maximum velocity occurs at the highest elevation. The velocity variations show different levels of complexity:

- The simplest shape is a straight line throughout the water column.
- The next level of complexity is two portions of equal number of data points that are collinear.
- A more complex shape is a combination of linear with nonlinear portions.

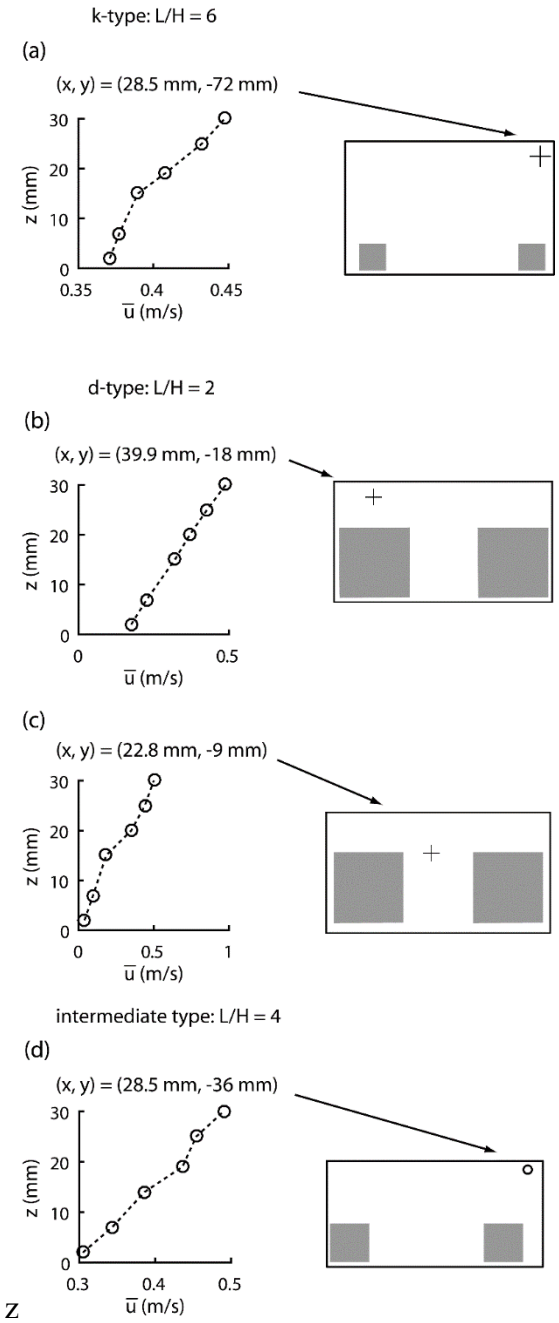

Figure 4.6 Linear or quasilinear profiles of $\bar{u}$ observed from the d-type, intermediate type, and k-type experiments. The horizontal locations of the observations are marked as: (a) the plus symbol '+', (b) the cross symbol '×', (c) the circle 'o', and (d) the square '□', where the approach flow is from right to left.

- Some profiles are purely nonlinear variations, often with a sudden increase in velocity immediately from the bed.
- Some profiles show flow separation from the bed.

An important implication is that a simple formulation of the bottom boundary condition in numerical models for simulations of turbulent flow over a roughness surface will not be adequate.

4.2 Turbulent shear stress

In typical analysis of turbulent boundary layer, the most interesting component of the specific turbulent shear stresses is given in Equation (2.11). Using the ADV measurements, we determined this component of the turbulent shear stresses as

$$\tau = -\frac{\rho}{N}\sum_{i=1}^{N}(u-\bar{u})(w-\bar{w}) \tag{4.1}$$

We plot the variations of τ with vertical distance, z, as vertical profiles. Based on the variations above the top of cubes, the shapes of the profiles can be classified into five different types (Type 1, 2, 3, 4, and 5), which are shown in Figures 4.7 throughout 4.11, respectively. In the figures, the centerline of the center row of cubes is aligned with the channel centerline**;** the normalized vertical distance by the roughness height is listed in Table 3.1, ranging from 0.105 to 1.630.

4.2.1 Type 1 profiles of turbulent shear stress

The main feature of Type 1 τ profiles (Figure 4.7a–f) is that the turbulent shear stress decreases with increasing height from the top of cubes (z > h, Figure 2.1 and 2.3). Such decrease is seen from classical boundary layer flow. The decrease shows a liner or approximately linear trend. Type 1 τ profiles were observed from all three types of surface roughness (the k-type, intermediate type, and d-type roughness). Within Type 1 τ profiles, there are differences in the distributions of τ

within the cavity or blow the top of cubes (or $z < h$), depending on the proximity to the cubes as well as the pitch ratio. Some specific details are highlighted below:

In Figure 4.7a, at $z < h$, the shear stresses at (x, y) = (-79.8 mm, -22.5 mm) are nonlinearly distributed, with the shear stress at the second lowest elevation smaller than that of at the lowest elevation. In fact, the maximum stress is at the lowest elevation. The minimum shear stress appears at $z = 31$, and the maximum value occurs at $z = 2$ mm. In Figure 4.7b, at the low elevations (at $z =$

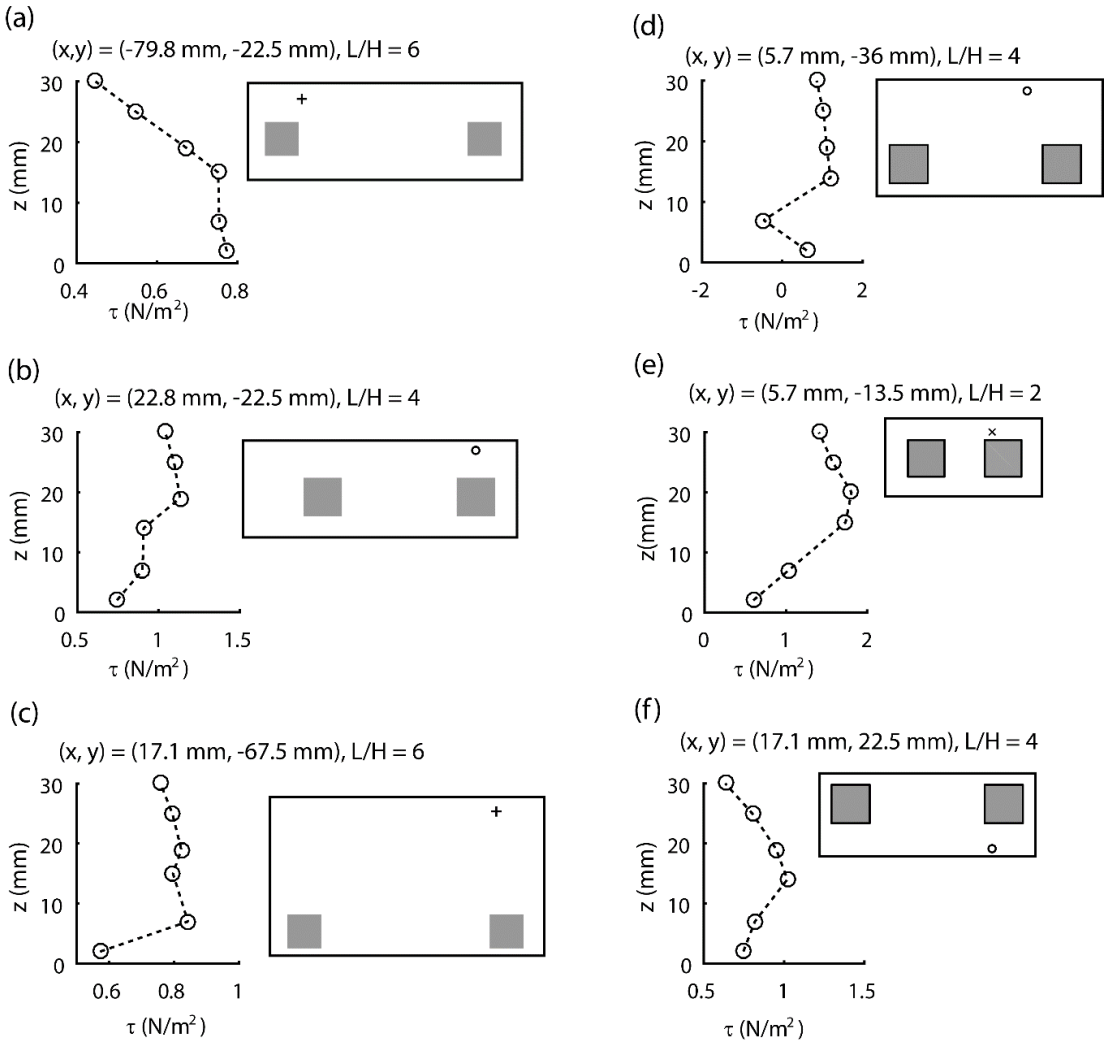

Figure 4.7 Type 1 profiles of turbulent shear stress, τ, (Equation 4.1) observed from the d-type, intermediate type, and k-type experiments, showing a decreasing shear stress with increasing height from the top of cubes. The locations of the measurements are marked by the symbols in the inert panels.

2, 7, 14 mm), the shear stresses are nonlinearly distributed. τ increases with vertical distance above the bed. In Figure 4.7c, the turbulent shear stresses are nonlinearly distributed at z = 2, 7, and 15 mm). The minimum shear stress appears at the lowest elevation, with a sudden increase at the second lowest elevation, in contrast to a sudden decrease in Figure 4.7d. In Figures 4.7e-f, at the three low elevations (z = 2, 7, 14 mm), τ increases linearly as elevation rises.

4.2.2 Type 2 profiles of turbulent shear stress

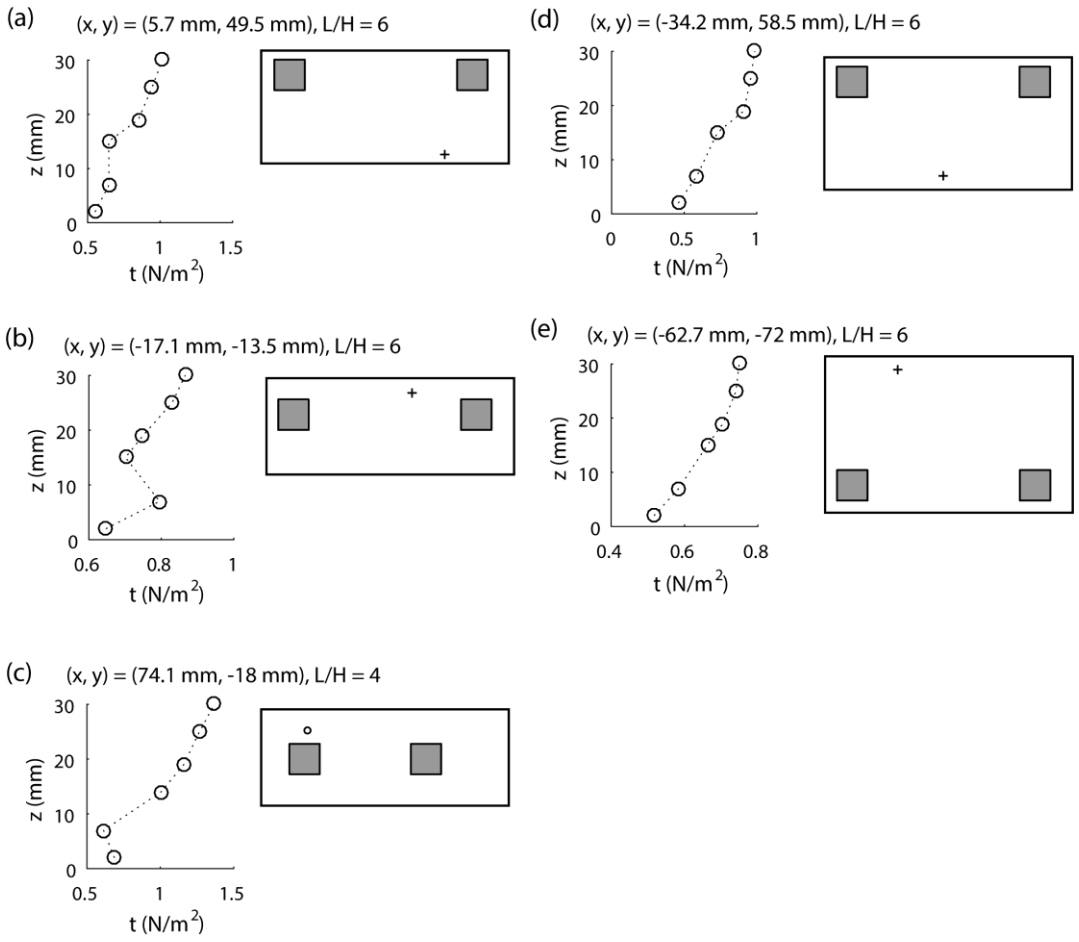

Figure 5.8 Type 2 profiles of turbulent shear stress, τ, (Equation 4.1) observed from the intermediate type and k-type experiments, showing an increasing shear stress with increasing height from the top of cubes. The locations of the measurements are marked by the symbols in the inert panels.

As illustrated in Figures 8a–e, Type 2 τ profiles feature an increase in the turbulent shear stress, τ, with *z* above the top of cubes. The increase is weakly nonlinear for z > h (Figure 2.1 and 2.3). The weakly nonlinear increase is also true for the cavity (z < h) in Figures 4.8a,d,e. In Figures 4.8b,c, the shear stress τ shows spatial fluctuations in the cavity.

4.2.3 Type 3 profiles of turbulent shear stress

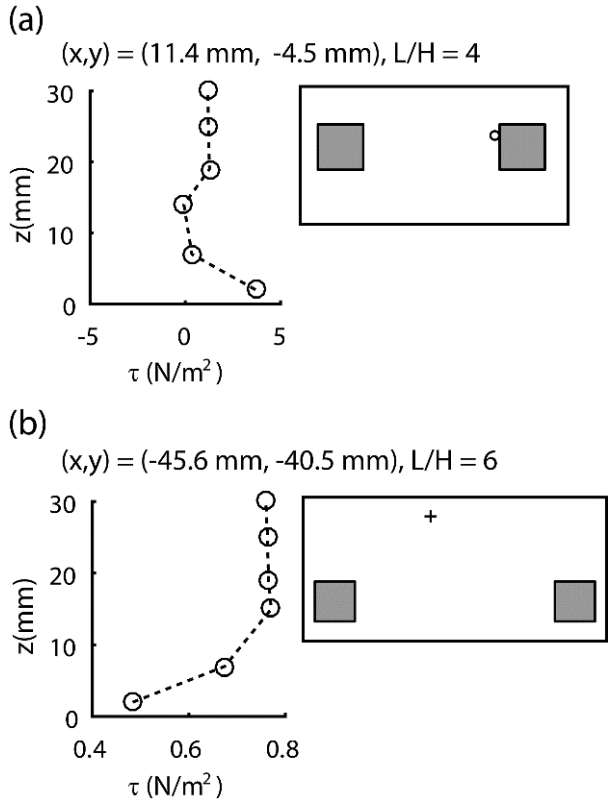

Figure 4.9 Type 3 profiles of turbulent shear stress, τ, (Equation 4.1) observed from the intermediate type and k-type experiments, showing essentially constant shear stress above the top of cubes. The locations of the measurements are marked by the symbols in the inert panels.

The main characteristics of Type 3 profiles of the turbulent shear stress is that τ has more or less a constant value above the level of the top of cubes, as illustrated in Figure 4.9a,b. Such profiles

were observed from the intermediate type and k-type surface roughness. In Figure 4.9a, the value of τ is shown to drop suddenly at z = 7 mm from that at z = 2 mm. In Figure 4.9b, τ increases nonlinearly with vertical distance from z = 2 mm to z = 15 mm.

4.2.4 Type 4 profiles of turbulent shear stress

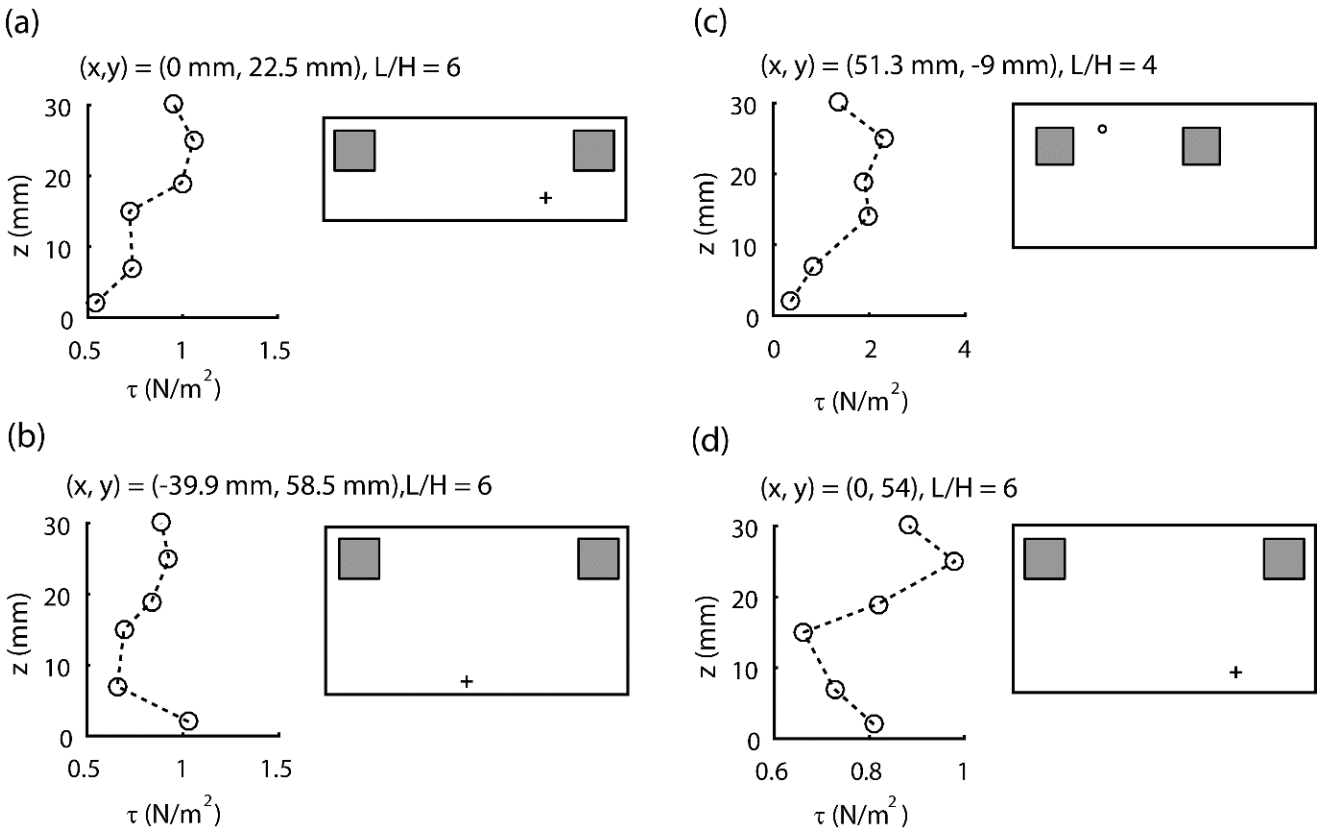

Figure 4.10 Type 4 profiles of turbulent shear stress, τ, (Equation 4.1) observed from the intermediate type and k-type experiments, showing a local maximum of τ above the top of cubes. The locations of the measurements are marked by the symbols in the inert panels.

Type 4 profiles (Figure 4.10a–d) of the turbulent shear stress have an S-shape. The profiles show a local maximum above the level of the top of cubes. That is to say that τ has a larger value at the

second highest elevation than at the data points above and below. The profiles shown in the figures were observed from the intermediate type and k-type experiments. The variations in τ are nonlinear in the entire water column, both below and above the level of the top of cubes. The profile shown in Figure 4.10d has a zig-zag shape, which appears to be piecewise linear.

4.2.5 Type 5 profiles of turbulent shear stress

Similar to Type 4 profiles, Type 5 profiles (Figure 4.11a–c) of the turbulent shear stress, τ, have an S-shape. Type 5 profiles show that τ has a local minimum above the level of top of cubes, which is different from Type 4 profiles (Figures 4.10a–d).

In Figure 4.11a, the profile of τ shows entirely nonlinear distributions. Below the level of the top of cubes (at z = 2, 7, 15 mm), τ has the minimum value at the lowest elevation and increases suddenly at the second highest elevation. The magnitude of τ is lower at the second highest elevation (z = 25 mm) than at the third highest elevation (z = 19 mm). In Figure 4.11b, below the level of the top of cubes, the shear stress is lower at the second lowest elevation (z = 7 mm) than at the lowest elevation (z = 2 mm). At the relatively higher elevations, the variations of τ shows zig-zag shapes. In Figure 4.11c, below the level of the top of cubes, the variations of τ are approximately linear; τ decreases linearly at higher elevations rises, and reaches the minimum value at the third lowest elevation.

It is concluded that the turbulent shear stress, τ, exhibits five different types of distributions. All the distributions are of nonlinear shapes when the water column is taken into account. Above the level of the top of cubes, Type 1 profiles show a shape of monotonically decreasing τ values toward higher elevations from the bed. Type 2 profiles show a trend of monotonically increasing τ values toward higher elevations. Type 3 profiles show essentially constant τ values. Type 4

profiles show a maximum of τ values. Type 5 profiles show a minimum of τ values. Below the level of the top of cubes, the variations of τ have a verity of different patterns including linear variations, weakly nonlinear variations, and zig-zag variations.

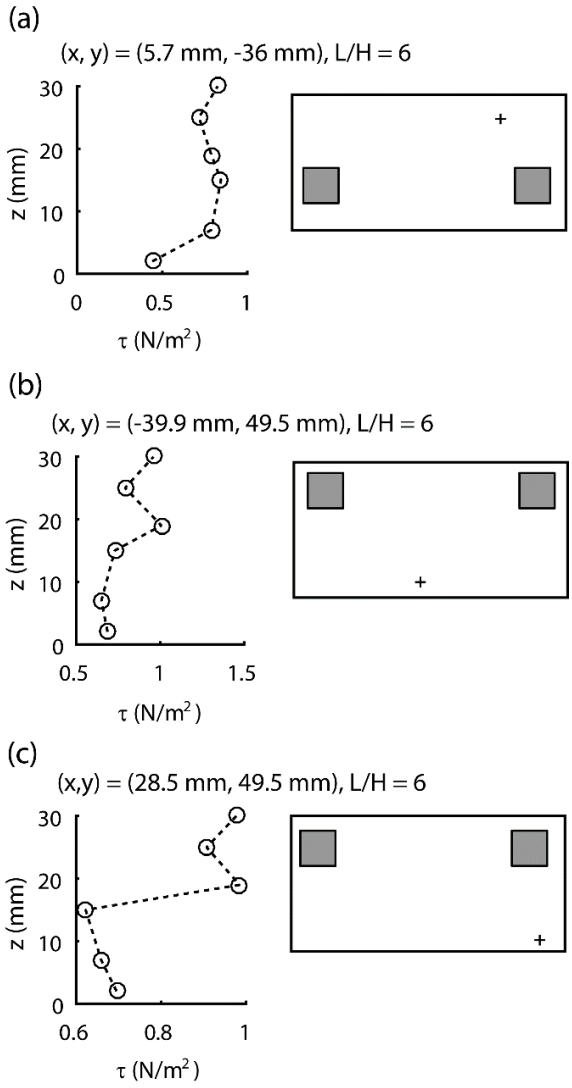

Figure 4.11 Type 4 profiles of turbulent shear stress, τ, (Equation 4.1) observed from the intermediate type and k-type experiments, showing a local maximum of τ above the top of cubes. The locations of the measurements are marked by the symbols in the inert panels.

4.3 Comparison between measured velocity and logarithmic velocity distributions

The flow velocity, $\bar{u}$, measured from the d-type, intermediate type and k-type experiments, has a verity of vertical variations, depending on the locations of measurements, as shown in Figures 4.1–4.6. In general, these vertical variations do not follow the theoretical logarithmic distribution of flow velocity, given in Equation 2.21 for a smooth bed, and Equation 2.22 for a rough bed. It would be constructive to provide quantitative comparisons between the measured velocities and theoretical values.

We investigate whether or not the vertical structure of the flow above the d-type roughness surface is such that the surface can be treated as a smooth surface. To do so, we calculate the friction velocity, u_*, in Equation (2.21) using the measured turbulent shear stress $\rho\tau_{xz}$ (Equation 2.11) at the elevation of z = 0.020 m. Then, we calculate the longitudinal flow velocity as

$$\bar{u} = \mathrm{u}_* \left[2.5 \ln\left(\frac{z-0.020}{\nu/u_*}\right) + 5.1\right] \tag{4.2}$$

at the elevations of z = 0.025 m and 0.031 m. The measured and calculated values of $\bar{u}$ are compared in Table 4.1. As expected, there are large relative errors. This leads to the conclusion that even the d-type roughness surface cannot be simplified as a smooth surface.

For the intermediate type and k-type surface roughness, the differences of velocity distributions from the theoretical distributions (Equation 2.21 or 2.22) are even larger.

Table 1.1 Comparisons between measured and theoretical values of $\bar{u}$ for the d-type roughness. The turbulent shear stress, τ, is the elevation of z = 15 mm. The measured and theoretical values of $\bar{u}$ in the parenthesis are at the elevations of z = 20, 25 and 31 mm.

x	y	τ	u_*	Measured $\bar{u}$		Theoretical $\bar{u}$		Relative error	
(mm)	(mm)	(N/m^2)	(m/s)	at z = 25 mm	at z = 31 mm	at z = 25 mm	at z = 31 mm	at z = 25 mm	at z = 31 mm
0	12	1.920	0.044	0.471	0.503	0.814	0.900	73%	73%
0	-12	1.979	0.044	0.434	0.486	0.828	0.916	91%	91%
5	20	1.515	0.039	0.473	0.547	0.711	0.788	50%	50%
5	-20	1.860	0.043	0.412	0.481	0.799	0.884	94%	94%
10	4	1.617	0.040	0.450	0.516	0.738	0.817	64%	64%
10	-4	1.677	0.041	0.439	0.515	0.754	0.834	72%	72%
15	4	2.315	0.048	0.443	0.519	0.905	1.000	104%	104%
15	-4	2.018	0.045	0.448	0.511	0.837	0.926	87%	87%
20	12	2.415	0.049	0.459	0.525	0.927	1.024	102%	102%
20	-12	1.732	0.042	0.454	0.505	0.768	0.850	69%	69%
25	8	1.584	0.040	0.461	0.524	0.730	0.808	58%	58%
25	-8	2.256	0.048	0.445	0.506	0.892	0.985	101%	101%
30	20	1.562	0.040	0.470	0.534	0.724	0.802	54%	54%
30	-20	1.846	0.043	0.427	0.484	0.796	0.881	86%	86%
35	20	1.598	0.040	0.487	0.534	0.733	0.812	51%	51%
35	-20	1.624	0.040	0.429	0.417	0.740	0.819	72%	72%

4.4 Secondary flow

Secondary flow in open-channel is defined as the movement of water particles on a cross section normal to the longitudinal direction of the channel (Chow 1959). The secondary flow can develop in open-channels of various shapes including rectangular, triangular, trapezoidal and circular channels. The intensity of secondary flow, U_s, is given in Equation (2.16). A high intensity corresponds to high energy loss in open-channel flow. For this reason, secondary flow is considered as channel resistance. This section discusses the effect of surface roughness on U_s.

4.4.1 Secondary flow intensity in the yz-plane

The yz-plan is a vertical cross section across the channel width (Figure 3.1) at a given *x* coordinate (Figures 3.5, 3.6, and 3.7). U_s at selected cross sections is discussed below.

4.4.1.1 d-type surface roughness

For the d-type roughness experiments, five cross sections, located at x = 0, 5.7, 11.4, 17.1, 34.2 mm (Figure 3.5), respectively, are selected to show U_s distributions as contour plots (Figures 4.12a–e). The normalized vertical distance by the roughness height is listed in Table 3.1, ranging from 0.105 to 1.577. In these plots, the dashed line indicates the elevation of the cube top at z = 19 mm (the same hereafter). In Figures 4.12a and 4.12e, the cross sections laterally cross a cube. Relatively high U_s is seen below the dashed line, near the cube's left edge (at y = -10 mm), and directly above the cube top. At the other three cross sections (Figures 4.12b–d), relatively high U_s occurs below the dashed line.

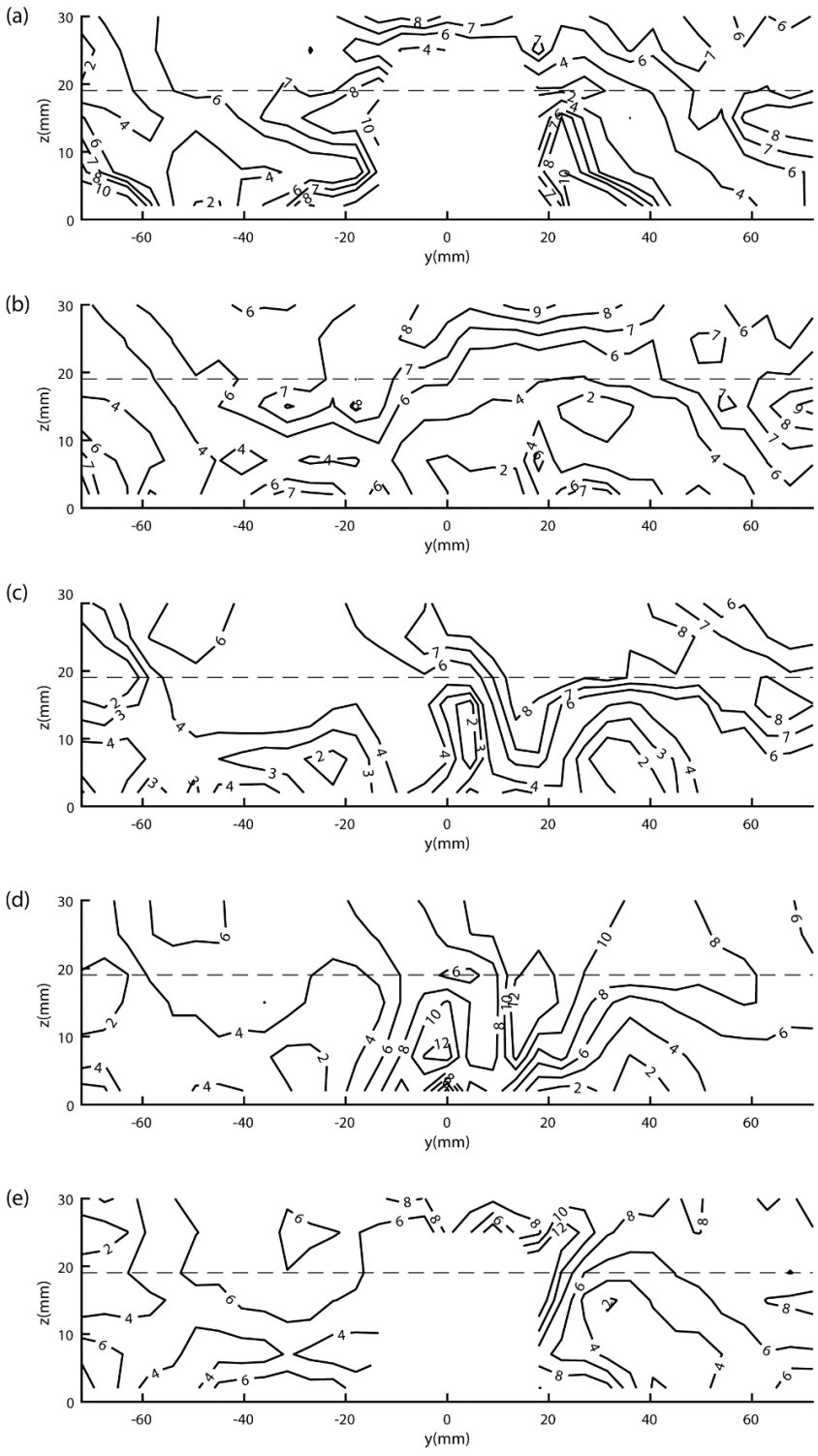

Figure 4.12 Distributions of secondary flow intensity, Us, (in percentage) at vertical cross sections located at x equal to: (a) 0 mm; (b) 5.7 mm; (c) 11.4 mm; (d) 17.1 mm; (e) 34.2 mm.

In Figure 4.12a, a region of relatively high U_s occurs where $y \leq -10$ mm to the left of the cube. This region is bounded by 10 mm $\leq z \leq$ 18 mm and -16 mm $\leq y \leq$ -13 mm. U_s decreases in the positive and negative z-direction, from a maximum of 7% at the elevation of z = 15 mm to a minimum of 2% at z = 30 mm and z = 2 mm. Also it decreases in the negative y-direction from 7% at y = -13 mm to 3% at y = -25 mm. In the central area (-10 mm $\leq y \leq$ 14 mm), relatively strong U_s appears directly above the cube, bounded by 28 mm $\leq z \leq$ 30 mm and -3 mm $\leq y \leq$ 2 mm. U_s decreases in the negative z-direction, from 3% at z = 30 mm to 2% at z = 19 mm, and in the lateral direction from 3% at y = 0 to 2% at y = -10 mm and y = 13 mm. In the area of $y \geq 10$ mm, relatively strong U_s occurs in $z \geq 19$ mm. It decreases in the negative z-direction, from 3% at z = 19 mm to 2% at z = 2 mm.

In Figure 4.12b, two regions of relatively strong U_s appear below the dashed line: One is bounded by 16 mm $\leq z \leq$ 18 mm and 2 mm $\leq y \leq$ 7 mm, where U_s decreases from a maximum of 5% at z = 16 mm to 2% at z = 19 mm. The other is near the cube's left edge (at y = 10 mm), bounded by 2 mm $\leq z \leq$ 10 mm and 10 mm $\leq y \leq$ 14 mm. U_s decreases from 5% at z = 2 mm to 3% at z = 19 mm. In the positive y-direction, U_s drops from 5% at y = 14 mm to 3% at y = 20 mm. Relatively weak U_s occurs in 20 mm $\leq y \leq$ -12 mm, with an intensity of 3% below the dashed line and 2% above. Weak U_s appears in the area of -20 mm $\leq y \leq$ 20 mm above the dashed line and in the area below the dashed line on the right edge (at y = 10 mm) of the cube.

In Figure 4.12c, two regions of relatively strong U_s appear at about y = 4 mm below the dashed line near the bed. One region is bounded by 2 mm $\leq z \leq$ 9 mm and -7 mm $\leq y \leq$ 2 mm. U_s drops in the positive z-direction, from a maximum of 8% at the elevation of z = 2 mm to 2% at z = 30 mm. Also, U_s drops in the lateral direction from 8% at y = -5 mm to 1% at y = -18 mm and to 3% at y = 4 mm. The other region is bounded by 2 mm $\leq z \leq$ 11 mm and 6 mm $\leq y \leq$ 11 mm.

U_s drops in the positive z-direction, from 8% at z = 9 mm to 2% at z = 25 mm, and in the lateral direction, from 8% at y = 9 mm to 3% at y = 14 mm and to 2% at y = 20 mm.

In Figure 4.12d, a core of relatively strong U_s is bounded by 2 mm ≤ z ≤ 10 mm and -9 mm ≤ y ≤ 3 mm, symmetrical at about y = -4 mm. The center of the core is located at (y, z) = (-4 mm, 7 mm). U_s drops radially, in the lateral direction from a maximum of 12 % at y = -4 mm to 2% at y = ±20 mm, and in the vertical direction from 12% at the elevation of z = 7 mm to 4% at z = 2 mm and to 2% at z = 30 mm.

Table 4.2 A summary of regions of relatively high secondary flow intensity at five selected vertical cross sections of given x coordinates for the d-type roughness.

x	y	z	Maximum U_s	(y, z) of the maximum U_s	Figure
(mm)	(mm)	(mm)	(%)	(mm, mm)	
0	-16 ≤ y ≤ -13	10 ≤ z ≤ 18	7	(-13, 15)	4.12a
0	-3 ≤ y ≤ 2	28 ≤ z ≤ 30	3	(0, 30)	4.12a
0	y ≤ 10	z ≤ 19	3	(10, 19)	4.12a
5.7	16 ≤ y ≤ 18	2 ≤ z ≤ 7	5	(5, 16)	4.12b
5.7	10 ≤ y ≤ 14	2 ≤ z ≤10	5	z = 2	4.12b
5.7	-20 ≤ y ≤ 20	z ≤ 19	2	(0, 30)	4.12b
11.4	-7 ≤ y ≤2	2 ≤ z ≤ 9	8	(-5, 2)	4.12c
11.4	6 ≤ y ≤ 11	2 ≤ z ≤ 11	8	(14, 25)	4.12c
22.8	-9 ≤ y ≤ 3	2 ≤ z ≤10	12	(-4, 7)	4.12d
34.2	-15 ≤ y ≤ -13	7 ≤ z ≤12	4	(-13, 10)	4.12e

In Figure 4.12e, a region of relatively strong U_s occurs to the left (y ≤ -10 mm) of the cube, bounded by 7 mm ≤ z ≤ 12 mm and -15 mm ≤ y ≤ -13 mm. U_s decreases in the positive z-direction, from 4% at z =10 mm to 2% at z = 19 mm, and in the negative y-direction from 4% at y = -13 mm to 2% at y = -20 mm.

4.4.1.2 Intermediate-type surface roughness

For the intermediate type roughness experiment, contours of the secondary flow intensity, U_s, at five cross sections (at x = 0, 11.4, 22.8, 40, and 45 mm, respectively, see Figure 3.7) are plotted in Figures 4.13a–e. The normalized vertical distance by the roughness height is listed in Table 3.1, ranging from 0.105 to 1.577. Two (Figures 4.13a,e) of these cross sections cross a cube, where two regions of relatively strong U_s appear below the dashed line near the cube's two sides (y = ± 10 mm). The other cross sections each show relatively strong U_s below the dashed line in three regions, which are nearly symmetrical about the channel centreline (at y = 0). In addition, they each show a region of relatively strong U_s at the elevation of the dashed line. This region is more or less symmetrical about y = 0.

In Figure 4.13a, relatively strong U_s appear in two regions below the dashed line: 1) one bounded by 15 mm ≤ y ≤ 20 mm and 2 ≤ z ≤ 12 mm, near the cube's right side (y = 10 mm); 2) the other bounded by -17 mm ≤ y ≤ -13 mm and 2 mm ≤ z ≤ 19 mm. U_s decreases in the negative y-direction from 5% at y = -13 mm to 2% at around y = -20 mm. Above the dashed line, U_s is weak in the area of y ≤ -12 mm. In Figure 4.13b, there are two regions, symmetrical about y = 0, of relatively strong U_s. One is below the dashed line, bounded by -20 mm ≤ y ≤ 22 mm and 2 ≤ z ≤ 14 mm, centred at (y, z) = (0 mm, 7 mm). U_s decreases radially, in the positive z-direction from 8% at the elevation of z = 2 mm to 5% at z = 14 mm, and in the lateral direction from 8% at y = 0 to 4% at y = ± 27 mm. The other region is bounded by -5 mm ≤ y ≤ 5 mm and 17 ≤ z ≤ 24 mm, centred at (y, z) = (0 mm, 19 mm). U_s decreases radially, in the vertical direction from 7% at z = 19 mm to 2% at z = 14 mm, and to 4% at z = 30 mm, and laterally from 7% at y = 0 to 2% at y = 27 mm and to 3% at y = -26 mm. The regions where the secondary flow intensities are relatively

strong are summarised in Table 4.3 for the cross sections shown in Figures 4.13a,b, along with the cross sections shown in Figures 4.13c–e.

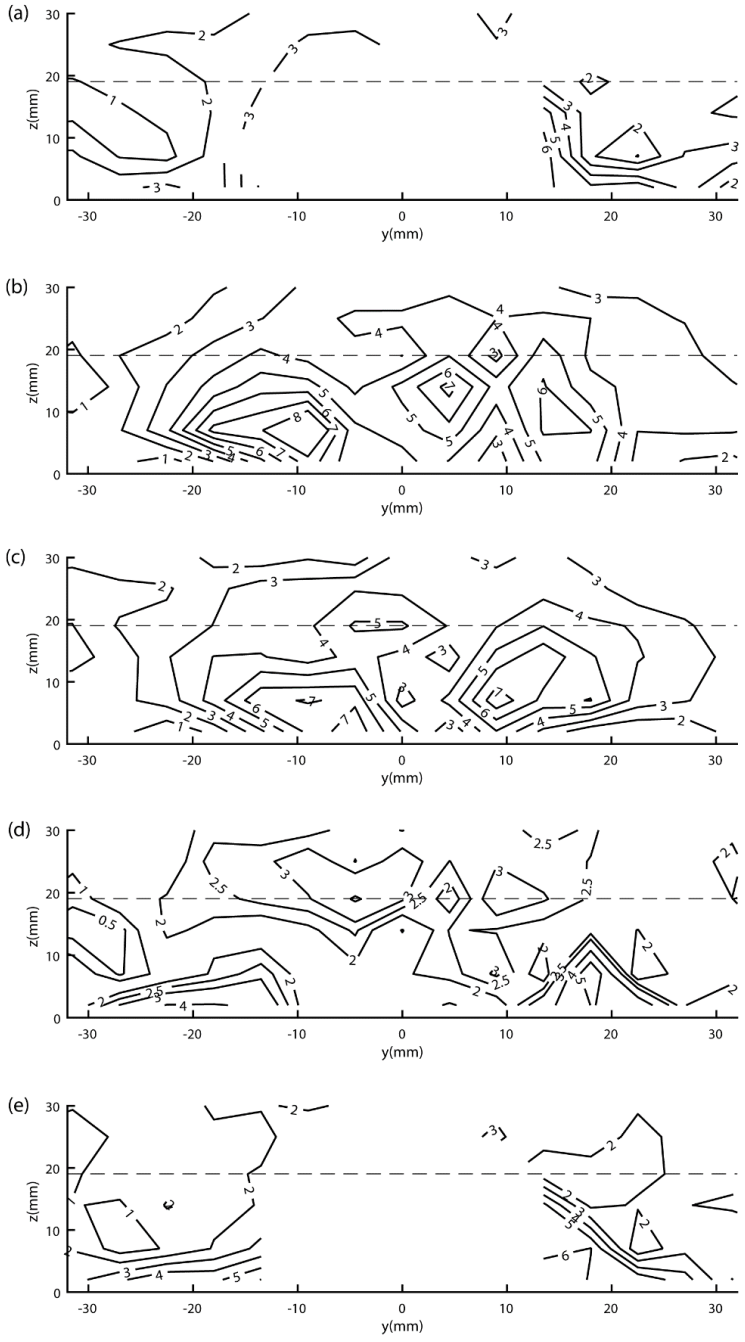

Figure 4.13 Distributions of secondary flow intensity (in percentage) at vertical cross sections located at x equal to: (a) 0 mm; (b) 11.4 mm; (c) 22.8 mm; (d) 40 mm; (e) 45 mm. The results are from the intermediate type roughness experiment.

Table 4.3 A summary of regions of relatively high secondary flow intensity at five selected vertical cross sections of given x coordinates for the intermediate type roughness.

x	y	z	Maximum U_s	(y, z) of the maximum U_s	Figure
(mm)	(mm)	(mm)	(%)	(mm, mm)	
0	$15 \leq y \leq 20$	$2 \leq z \leq 12$	6	(14, 10)	4.13a
0	$-17 \leq y \leq -13$	$2 \leq z \leq 19$	5	$y = -13$	4.13a
11.4	$-20 \leq y \leq -5$	$2 \leq z \leq 14$	8	(0, 7)	4.13b
22.8	$0 \leq y \leq 10$	$7 \leq z \leq 19$	7	(5, 19)	4.13c
28.5	$14 \leq y \leq 24$	$2 \leq z \leq 11$	5	(18, 2)	4.13d
28.5	$-26 \leq y \leq -11$	$2 \leq z \leq 7$	4	$z = 2$	4.13d
28.5	$-12 \leq y \leq 2$	$15 \leq z \leq 25$	4	(-4, 19)	4.13d
34.2	$14 \leq y \leq 25$	$2 \leq z \leq 8$	7	(17, 5)	4.13e
34.2	$-25 \leq y \leq -14$	$2 \leq z \leq 8$	5	$z = 2$	4.13e

4.4.1.3 k-type surface roughness

For the k-type roughness experiment, contours of the secondary flow intensity, U_s, at five cross sections (at x = 20, -5, -25, -45, and -75 mm, respectively, see Figure 3.6) are plotted in Figures 4.14a–e. The normalized vertical distance by the roughness height is listed in Table 3.1, ranging from 0.105 to 1.577.

The cross section at x = 20 (Figure 4.14a) crosses a cube. This cross section shows a region of relative high U_s above the dashed line, bounded by $-12 \text{ mm} \leq y \leq 12 \text{ mm}$ and $25 \text{ mm} \leq z \leq 30$ mm. High intensities are $U_s = 8\%$ at z = 30 mm, and $U_s = 7\%$ at y = -20 mm. Below the dashed line and $y \leq 12$ mm, there is a region of relatively strong U_s, bounded by $-20 \text{ mm} \leq y \leq -12$ mm and $2 \text{ mm} \leq z \leq 19$ mm. This region can be divided into two centres: one located at z = 17 mm,

and the other at z = 5 mm. Above z = 7 mm, U_s decreases in the vertical direction from a local maximum of 10% at z = 17 mm to a local minimum of 6% at z = 19 mm and to 4% at z = 7 mm. U_s decreases in the negative y-direction from 10% at y = -12 mm to 6% at y = -50 mm. Below z = 7 mm, U_s drops in the positive z-direction from a local maximum of 10% at z = 2 mm to a local minimum of 4% at z = -7 mm, and in the negative y-direction from 10% at y = -12 mm to 2% at y = -50 mm.

In Figure 4.14a, above the dashed line and y > 12 mm, U_s decreases in the negative z-direction from 7% at z = 30 mm to 2% at z = 19 mm, and increases in the positive y-direction from a local minimum of 2% at y = 17 mm to a local maximum of 7% at y = 52 mm. Below the dashed line and y > 12 mm, there is a region of relatively strong U_s, bounded by 17 mm $\leq$ y $\leq$ 40 mm and 2 mm $\leq$ z $\leq$ 17 mm. The local maximum intensity is U_s = 10% at (y, z) = (24 mm, 2 mm). A summary of the regions of high U_s is given in Table 4.4.

In Figure 4.14b, the main feature is the occurrence of five cores of high secondary flow intensity: two near the bottom, centred at the elevation of z = 2 mm and at y = ± 30 mm, respectively, which are symmetrical about the channel centreline; one in the lower left corner; one next to the right channel-sidewall just below the level of the cube top; one above the level, centred at y = 20 mm approximately. The secondary flow intensity has local maxima of U_s = 7% in the two cores near the bottom, U_s = 8% in the corner core, U_s = 9% in the core next to the right sidewall and in the core above the level of the cube top. More details about the high Us regions are listed in Table 4.4.

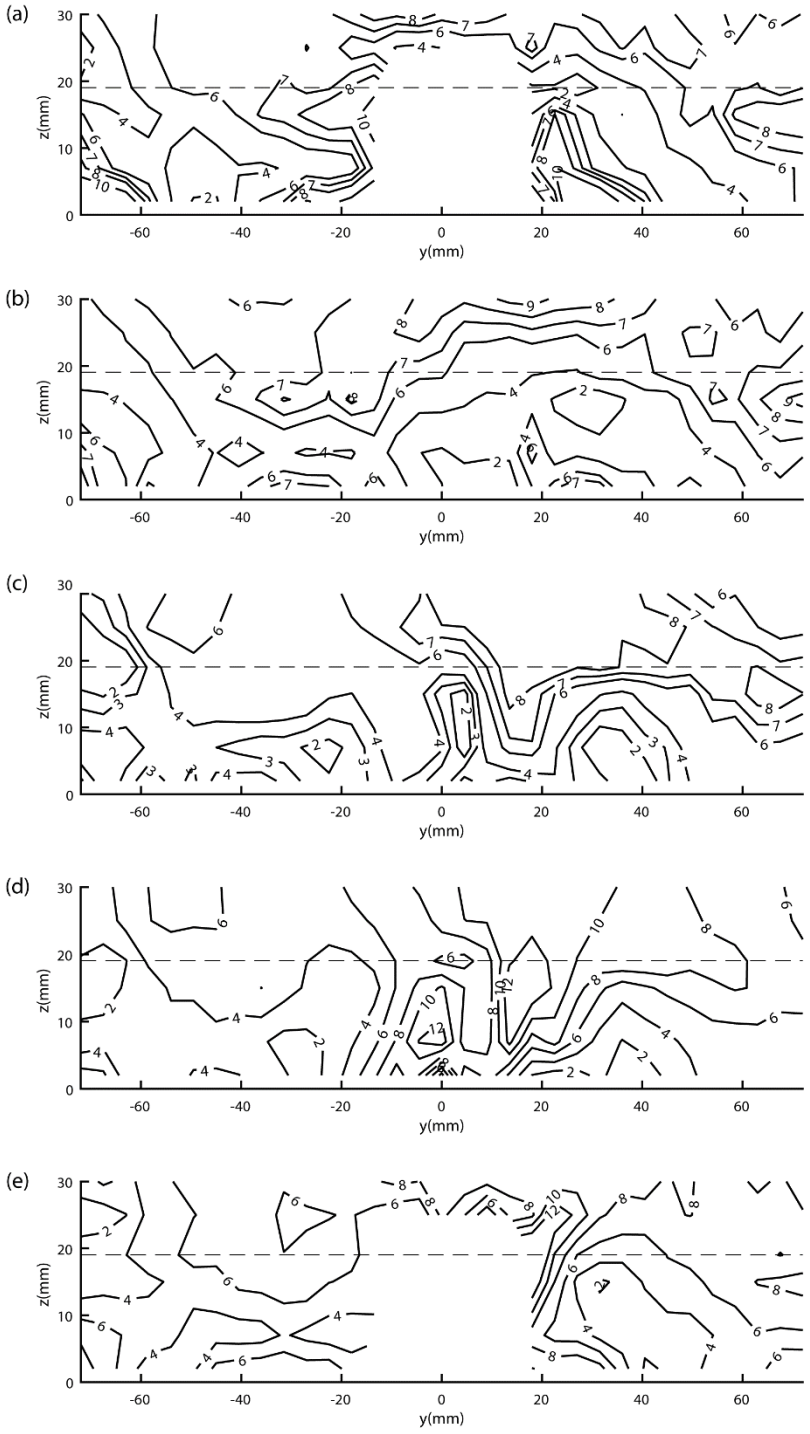

Figure 4.14 Distributions of secondary flow intensity (in percentage) at vertical cross sections located at x equal to: (a) 22.8 mm; (b) -5.7 mm; (c) -28.5 mm, (d) -51.3 mm; (e) -85.5 mm. The results are from the k-type roughness experiment.

Table 4.4 A summary of regions of relatively high secondary flow intensity at six selected vertical cross sections of given x coordinates for the k-type roughness.

x	y	z	Maximum U_s	(y, z) of the maximum U_s	Figure
(mm)	(mm)	(mm)	(%)	(mm, mm)	
22.8	$-12 \le y \le 12$	$25 \le z \le 30$	8	z = 30	4.14a
22.8	$-20 \le y$	$25 \le z \le 30$	7	y = -20	4.14a
22.8	$-20 \le y \le -12$	$7 \le z \le 19$	10	(-12,17)	4.14a
22.8	$-20 \le y \le -12$	$2 \le z \le 7$	10	(-12,5)	4.14a
22.8	$y \le 12$	$z \le 19$	7	z = 30	4.14a
22.8	$y \le 12$	$z \le 19$	7	y = 52	4.14a
28.5	$17 \le y \le 40$	$2 \le z \le 17$	10	(2,24)	4.14a
-5.7	$-36 \le y \le -12$	$14 \le z \le 19$	8	(-30, 17)	4.14b
-5.7	$-36 \le y \le -12$	$14 \le z \le 19$	8	(-20,17)	4.14b
-5.7	$-50 \le y \le -10$	$2 \le z \le 14$	7	(-30, 2)	4.14b
-5.7	$-10 \le y \le 40$	$25 \le z \le 30$	9	z = 30	4.14b
-5.7	$20 \le y \le 30$	$2 \le z \le 5$	9	(28,2)	4.14b
-28.5	$y \le -10$	$19 \le z$	7	-	4.14c
-28.5	$-5 \le y \le 45$	$19 \le z$	8	-	4.14c
-51.3	$-8 \le y \le 2$	$5 \le z \le 15$	12	(-2, 8)	4.14d
-85.5	$12 \le y \le 24$	$6 \le z \le 25$	15	(8,15)	4.14d
-85.5	$-40 \le y \le -20$	$19 \le z \le 30$	6	(-30, 25)	4.14e
-85.5	$-50 \le y \le -20$	$2 \le z \le 7$	6	z = 2	4.14e
-85.5	$-20 \le y \le 30$	$7 \le z \le 30$	12	(20, 19)	4.14e
-85.5	$20 \le y \le 40$	$2 \le z \le 7$	8	z = 2	4.14e

The cross section shown in Figure 4.14c (at x = -28.5 mm) is located at a longitudinal distance of 20 mm downstream of the cross section shown in Figure 4.14b. The distribution of secondary flow intensity, U_s, changes significantly between the two cross sections. Figure 4.14c shows two regions of low U_s near the bottom, in contrast to two regions of high U_s in Figure 4.14b. In addition, Figure 4.14c shows a downward intrusion of the high U_s region just to the left of y = 20 mm. Overall, U_s is high in the upper right quarter of the cross section (Figure 4.14c).

The downward intruding high U_s region just to the left of y = 20 mm intensifies at the cross section shown in Figure 4.14d, where Us has a local maximum of 12%, in comparison to 8% in Figure 4.14c. Also, in Figure 4.14d, a new core of high U_s with a local maximum of 12% appears at around z = 10 mm at the channel centreline (y = 0), which is in contrast to where is a low Us core in Figure 4.14c.

The cross sections shown in Figures 4.14e and 4.14a both cross a cube, but the distributions of U_s are different between the two cross sections. To the left of the cube, U_s is not as high as in the former than in the latter, and is more uniform in the former than in the latter. To the right of the cube, Figure 4.14e shows high U_s above the cube top. A summary of the high U_s regions is provided in Table 4.4.

In summary, the k-type roughness experiment produces secondary flow that has largely different distributions at cross sections of different longitudinal locations. At a given longitudinal location, the secondary flow intensity, U_s, varies significantly from one subsection to another subsection. Regions of high U_s are symmetrical about the channel centreline at some cross section, but the general patterns are asymmetrical. In most of the cross sections, Us is higher on one side of the channel centreline than the other side.

4.4.2 Secondary flow intensity in the xy-plane

The xy-plan is a horizontal plane at a given *z* coordinate (Figure 3.4). In this section, the distributions of the secondary flow intensity, U_s (Equation 2.16), at three such planes are discussed. The distributions are based measurements from locations shown in Figure 3.5 for the d-type roughness, Figure 3.6 for the k-type roughness, and Figure 3.7 for the intermediate type roughness.

4.4.2.1 d-type surface roughness

For the d-type roughness, the distributions of U_s in three horizontal planes at z = 2, 14, and 25 mm, respectively, are plotted as contours in Figures 4.15a–c. A comparison among these figures indicates that U_s decreases with increasing height from the channel-bed. For example, U_s has a maximum value of 9% at z = 2 mm (Figure 4.15a), compared to 6% at z = 15 mm (Figure 4.15b) and 1.4% at z = 25 mm (Figure 4.15c). The flow at z = 2 and 15 mm is within the cavity of roughness elements, which cause the profound lateral and vertical movement of water particles, and thus give rise to high secondary flow intensity.

Note that the channel centreline is at y = 0, and the central row of cubes' sidewalls are at around y = ±10 mm, and the longitudinal centrelines between the central row of cubes and the adjacent row of cubes are at y = ± 20 mm (Figure 3.5). The primary flow is in the positive x-direction (or from the top to the bottom of the panel) in Figure 4.15a. This figure shows higher U_s around the upstream cube than around the downstream cube. This is to say that the structure of secondary flow is not spatially periodic between adjacent roughness elements in the longitudinal direction, in the vicinity of the channel-bed (at z = 2 mm). It is likely that the between element variations in the secondary flow are due to structural modes of length scales larger the cube spacing (Figure 2.1).

In Figure 4.15a, the region of relatively strong U_s downstream of the cube at upstream is bounded by -10 mm ≤ y ≤ 10 mm and 15mm ≤ x ≤ 25 mm. Us has local maximum values (equal to 3%) along the central longitudinal strips (at y = ±20 mm) between laterally adjacent roughness elements. More details about regions of relatively high U_s are given in Table 4.5.

At the elevation of z = 14 mm, the overall distributions of the secondary flow intensity, U_s, are approximately symmetrical about the channel centreline at y = 0 mm, as illustrated in Figure 4.15b. U_s is relatively high within the cavity space between the downstream face of the element at upstream and the upstream face of the element at downstream, compared to the intensity outside the space. U_s is relatively weak in the two regions at the upstream corners of the cube at downstream. At the elevation of z = 25 mm (above the cube top), U_s is low (Figure 4.15c). The distributions of U_s are asymmetrical about the channel centreline. Relatively speaking, U_s is more significant in the region bounded by -15 mm ≤ y ≤ 5 mm and -11.4 mm ≤ x ≤ 25 mm. Above the cube at downstream, there is a region of relatively strong U_s, bounded by -15 mm ≤ y ≤ 5 mm and 34 mm ≤ x ≤ 45.6 mm. In the strip of -20 mm ≤ y ≤ 20 mm, contours of U_s are kind of symmetrical about y = -5 mm. More details are included in Table 4.5.

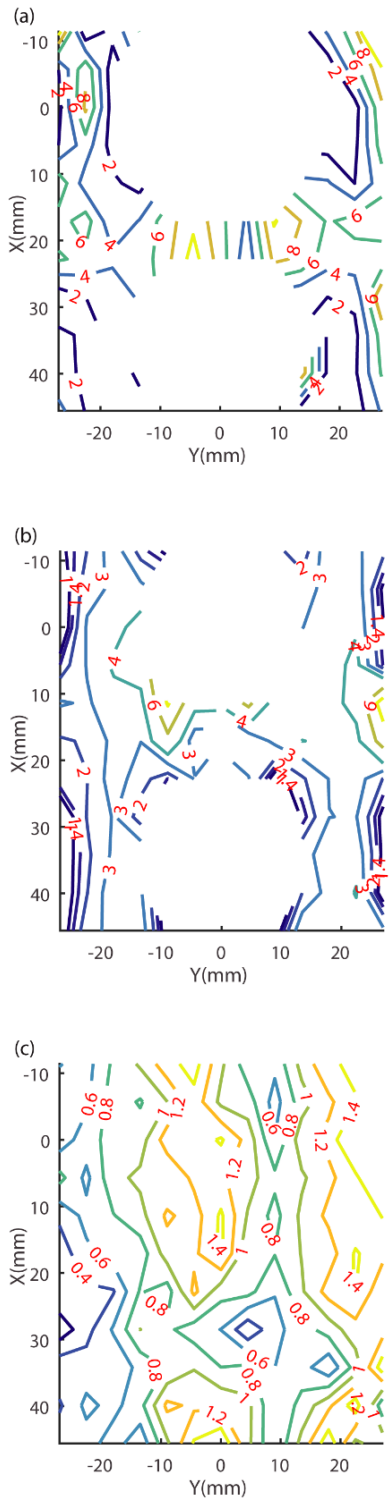

Figure 4.15 Distributions of secondary flow intensity (in percentage) in horizontal planes at the elevations of z equal to: (a) 2 mm (z /h = 0.105); (b) 15 mm (z/h = 0.789); (c) 25 mm (z/h = 1.314). The results are from the d-type roughness experiment.

Table 4.5 Regions of relatively high secondary flow intensity at three selected horizontal planes of given z coordinates for the d-type roughness.

z	x	y	Maximum U_s	(y, z) of the maximum U_s	Figure
(mm)	(mm)	(mm)	(%)	(mm, mm)	
2	$15 \leq x \leq 25$	$-10 \leq y \leq 10$	9	y = -5	4.15a
2	$32 \leq x \leq 45$	$-12 \leq y \leq 18$	8	(40, 12)	4.15a
15	$10 \leq x \leq 18$	$-10 \leq y \leq 10$	7	(10, -8)	4.15b
15	$10 \leq x \leq 18$	$-10 \leq y \leq 10$	6	(12, 5)	4.15b
25	$-11.4 \leq x \leq 25$	$-15 \leq y \leq 5$	1.4	(-11.4, -4)	4.15c
25	$-11.4 \leq x \leq 25$	$-15 \leq y \leq 5$	1.4	(0, 0)	4.15c
25	$-11.4 \leq x \leq 25$	$-15 \leq y \leq 5$	1.4	(12, 0)	4.15c
25	$-11.4 \leq x \leq 30$	$18 \leq y$	1.4	y = 20	4.15c
25	$40 \leq x \leq 45.6$	$-10 \leq y \leq 5$	1.4	x = 45.6	4.15c
25	$30 \leq x \leq 45.6$	$15 \leq y$	1.4	(45.6, 18)	4.15c
25	$30 \leq x \leq 45.6$	$15 \leq y$	1.4	(40, 22)	4.15c
25	$30 \leq x \leq 45.6$	$15 \leq y$	1.4	(34, 28)	4.15c

4.4.2.2 Intermediate-type surface roughness

For the intermediate type roughness, contours of the secondary flow intensity, U_s, in the horizontal planes at the elevations of z = 2, 14, and 25 mm, are plotted in Figures 4.16a-c, respectively. Note that the primary flow is in the negative x-direction or from the bottom to the top of the panels. In the vicinity of the channel-bed (z = 2 mm), the distributions manifest the geometric configurations of the roughness elements. The U_s contours are essentially symmetrical about the channel centreline at y = 0. Strong U_s appears around the four corners of a roughness element, in particular around the upstream corners. There is a region of weak U_s (at x = 50 mm) downstream of the roughness element next to the corners of strong U_s.

The secondary flow is less intense at the elevation of z = 14 mm (Figure 4.16b) than at z = 2 mm in the vicinity of the channel-bed (Figure 4.16a). In Figure 4.16b, high U_s contours hug the

downstream face of a roughness element. Two side-by-side cores of relatively high U_s form in the cavity space between two longitudinally adjacent roughness elements. The two cores are closer to the upstream face of the element at downstream. One shows somewhat higher U_s than the other. The positions of the two cores are more or less symmetrical about the channel centreline (at y = 0).

The secondary flow intensity, U_s, has lower values at the elevation of z = 25 mm (Figure 4.16c), compared to the values below it (Figures 4.16a,b). In Figure 4.16c, relatively high U_s occurs in the cavity space between two longitudinally adjacent roughness elements. Relatively high Us also occurs over the top of roughness elements.

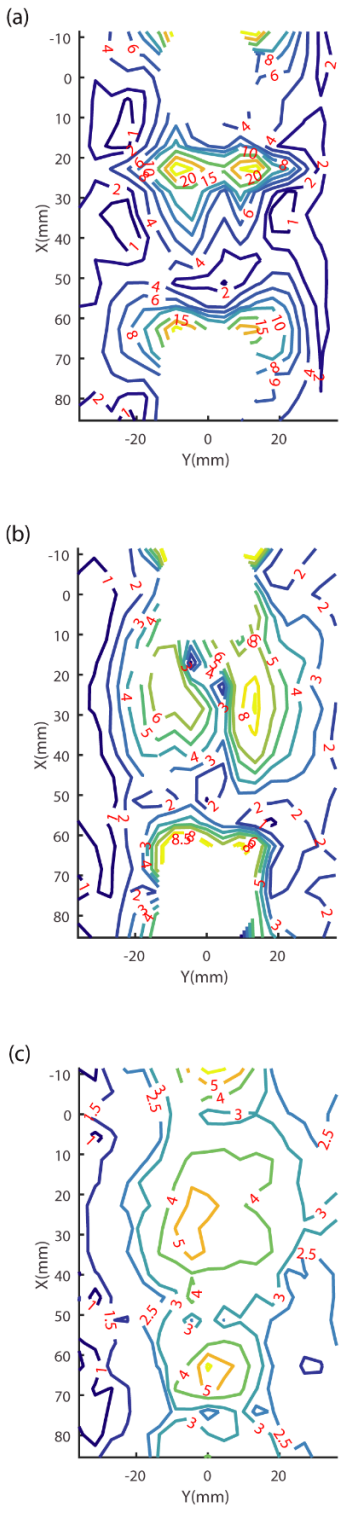

Figure 4.16 Distributions of secondary flow intensity (in percentage) in horizontal planes at elevations of z equal to: (a) 2 mm (z/h = 0.105); (b) 14 mm (z/h = 0.736); (c) 25 mm (z/h = 1.314). The primary flow is in the negative x-direction (or from the bottom to the top of the panels). The results are from the intermediate roughness experiment.

Table 2.6 Regions of relatively high secondary flow intensity at three selected horizontal planes of given z coordinates for the intermediate type roughness.

z	x	y	Maximum U_s	(x, y) of the maximum U_s	Figure
(mm)	(mm)	(mm)	(%)	(mm, mm)	
2	$20 \le x \le 25$	$-18 \le y \le 0$	25	(65, 10)	4.16a
2	$20 \le x \le 25$	$5 \le y \le 18$	25	(65, -10)	4.16a
2	$60 \le x \le 65$	$0 \le y \le 17$	25	(62, -10)	4.16a
2	$60 \le x \le 65$	$5 \le y \le 18$	15	(62, 10)	4.16a
14	$12 \le x \le 32$	$-18 \le y \le -2$	6	(10, 25)	4.16b
14	$20 \le x \le 32$	$10 \le y \le 20$	8.5	(26, 15)	4.16b
14	$58 \le x \le 68$	$-17 \le y \le 17$	8.5	(60, 5)	4.16b
14	$58 \le x \le 68$	$-17 \le y \le 17$	8	(62, 10)	4.16b
25	$-11.4 \le x \le -5$	$-10 \le y \le 10$	6	(-11.4, 0)	4.16c
25	$20 \le x \le 36$	$-10 \le y \le 2$	5	(28, -4)	4.16c
25	$60 \le x \le 70$	$-2 \le y \le 8$	6	(0, 62)	4.16c

4.4.2.3 k-type surface roughness

For the k-type surface roughness, contours of the secondary flow intensity, U_s, in horizontal planes at the elevations of z = 2, 15 and 25 mm are plotted in Figures 4.17a–c, respectively. These plots show that the U_s patterns are not connected between the two adjacent roughness elements in the longitudinal direction, and this is the case at all the three elevations. In other words, the secondary flow developing around the roughness element at upstream is isolated from that developing around the element at downstream. The individual roughness elements can be considered as an isolated element.

On the downstream face of a roughness element, the flow develops and behaves as a wake. Specially, at z = 2 mm, two side-by-side cores of strong U_s occur near the downstream corners of the roughness element at upstream (Figure 4.17a). One of the cores shows more profound U_s than the other. On the upstream side of a roughness element, two side-by-side cores of relatively high U_s form, symmetrical the channel centreline at y = 0. At z = 15 mm, two side-by-side cores of

strong U_s occur near the downstream corners of the element at upstream (Figure 4.17b). Between these two cores, U_s values have smaller disparity, compared to those two at z = 2 mm (Figure 4.17a). At z = 25 mm, two cores of relatively high U_s appear: one over the top of a roughness element, and the other between the adjacent roughness elements to right of the channel centreline. More data about the regions of profound U_s are given in Table 4.7.

In summary, it has been shown that the secondary flow intensity, U_s, is less profound at higher elevation. For example, for the d-type roughness, the maximum U_s drops from 20.37% at the elevation of z = 2 mm to 1.75% at z = 25 mm (Figures 4.15a–c). The k-type roughness causes the highest U_s near the water surface among the three types of surface roughness. For instance, U_s has a maximum value of 21.1% for the k-type roughness, 6.37% for the intermediate type roughness, and 1.75% for the d-type roughness.

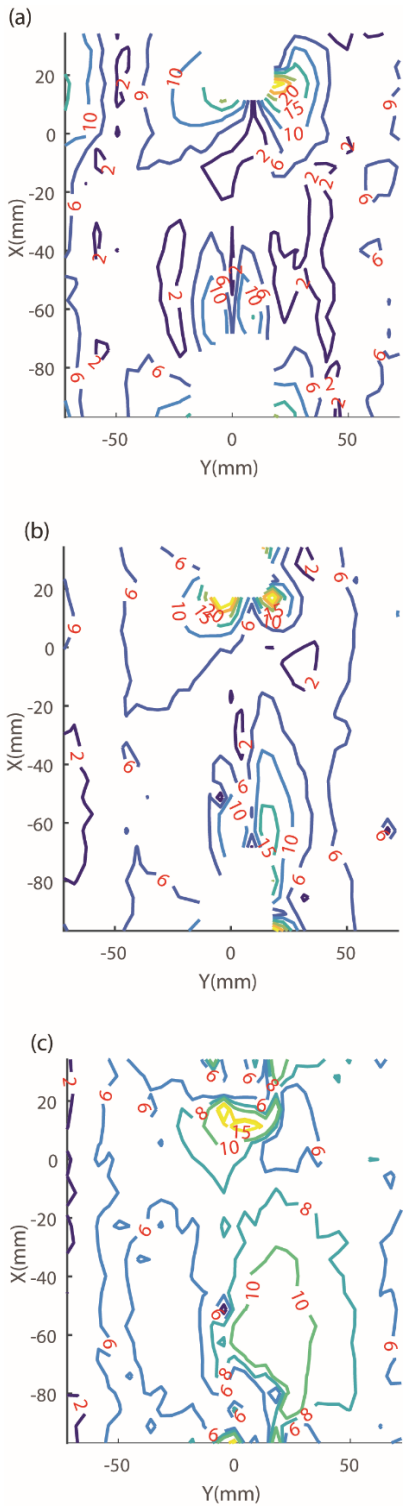

Figure 4.17 Distributions of secondary flow intensity (in percentage) in horizontal planes at elevations of z equal to: (a) 2 mm (z / h = 0.105); (b) 15 mm (z / h = 0.789); (c) 25 mm (z / h = 1.314). The primary flow is in the negative x-direction (or from the top to the bottom of the panels). The results are from the k-type roughness experiment.

Table 4.7 Regions of relatively high secondary flow intensity at three selected horizontal planes of given z coordinates for the k-type roughness.

z	x	y	Maximum U_s	(x, y) of the maximum U_s	Figure
(mm)	(mm)	(mm)	(%)	(mm, mm)	
2	$10 \leq x \leq 18$	$-12 \leq y \leq 4$	18	(12, -5)	4.17a
2	$20 \leq x \leq 25$	$14 \leq y \leq 26$	20	(16, 12)	4.17a
2	$-50 \leq x \leq -64$	$-12 \leq y \leq 0$	10	(-60, -5)	4.17a
2	$-50 \leq x \leq -64$	$0 \leq y \leq 15$	10	(-60, 5)	4.17a
15	$10 \leq x \leq 20$	$-10 \leq y \leq 25$	20	(18, 0)	4.17b
15	$10 \leq x \leq 20$	$-10 \leq y \leq 25$	20	(20, 14)	4.17b
15	$x \leq -50$	$-10 \leq y \leq 30$	10	(-60, -5)	4.17b
15	$x \leq -50$	$-10 \leq y \leq 30$	15	(-70, 15)	4.17b
25	$10 \leq x \leq 20$	$-10 \leq y \leq 10$	15	(15, 5)	4.17c
25	$-90 \leq x \leq -30$	$10 \leq y \leq 30$	10	(-60, -20)	4.17c

4.4.3 Secondary flow intensity in the xz-plane

To an observer facing the channel sidewalls (Figure 3.1), the xz-plane (Figure 2.1) is a vertical plane at a given *y* coordinate. The distributions of secondary flow intensity, U_s (Equation 2.16), in such vertical planes are shown in Figures 4.18a–g for the d-type roughness, in Figures 4.19a–i for the intermediate type roughness, and in Figures 4.20a–i for the k-type roughness. The dashed line in these figures mark the elevation of the top of roughness elements.

4.4.3.1 Secondary flow intensity at the channel centreline

The distributions of U_s in the channel-centreline plane ($y = 0$) are shown in Figures 4.18a, 4.19a and 4.20a, for the d-type, intermediate type, and k-type surface roughness, respectively. For the d-type roughness (Figure 4.18a), a curve of $U_s = 2\%$ is seen to remain as a continuous curve above the top of consecutive roughness elements. Below the top within the cavity, a localised packet of

high U_s forms close to the upstream face of an element. An important point is that there is a lack of interactions of secondary flow between the cavity and overlying regions.

This is not the case for the intermediate type roughness (Figure 4.19a). From this figure, it is clear that the secondary flow has coherent structures across the dashed line. This is also the case for the k-type roughness (Figure 4.20a). In other words, for these two types of surface roughness, the resultant secondary flow interacts between the cavity and overlying regions. In addition, the intermediate type roughness produces higher U_s than the d-type roughness, and thus more resistance to the primary flow. For the k-type roughness, a large region of low U_s exists within the cavity, which separates the structures of high U_s created around the roughness element at upstream and that at downstream. Due to such separation, the individual roughness elements are effectively an isolated element.

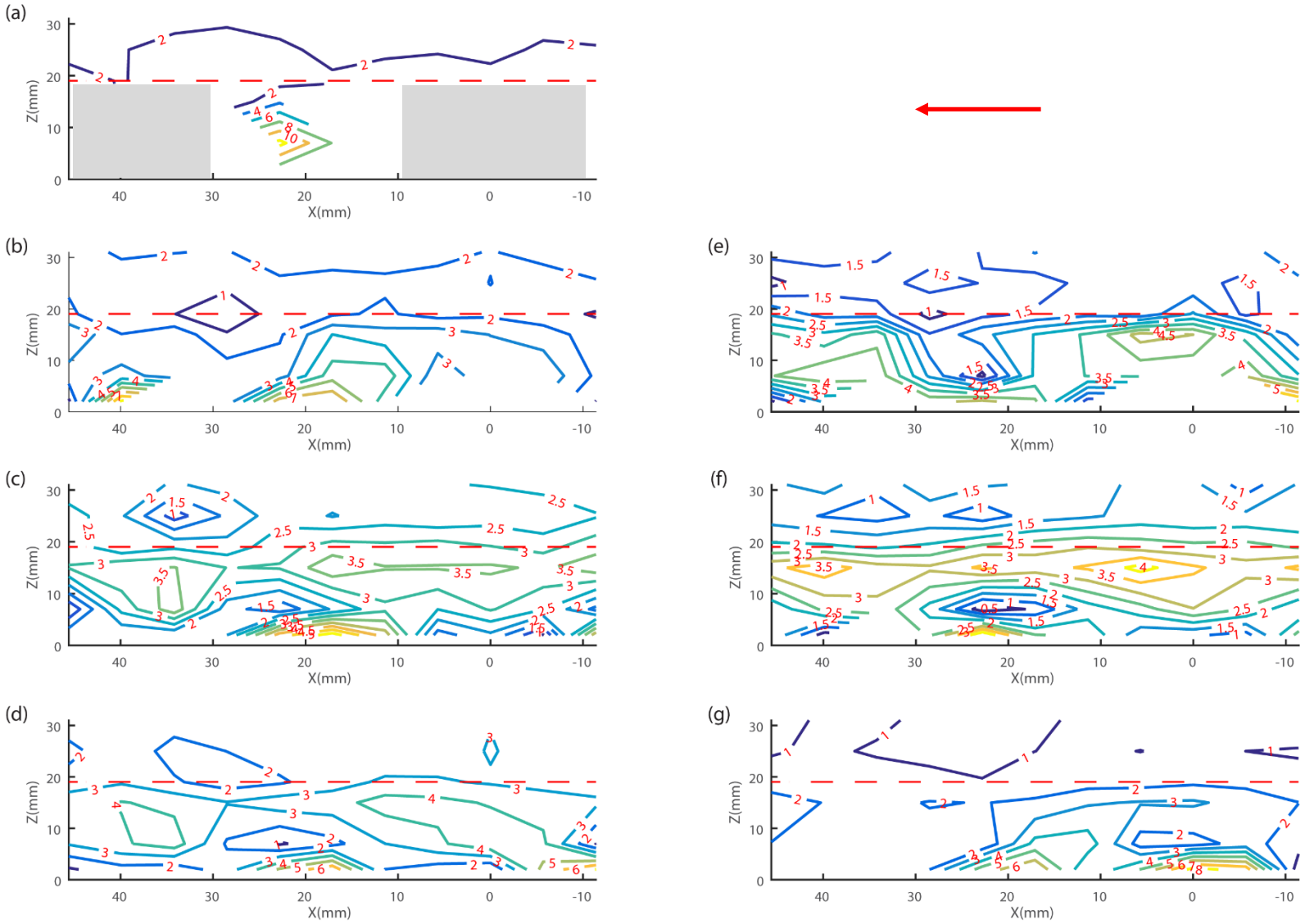

Figure 4.18 Contours of the secondary flow intensity (%) in vertical planes at y equal to: (a) 0; (b) 13.5; (c) 18; (d) 22.5, (e) -13.5; (f) -18; (g) -22.5 mm. The results are for the d-type roughness. The primary flow is from right to left (the red arrow).

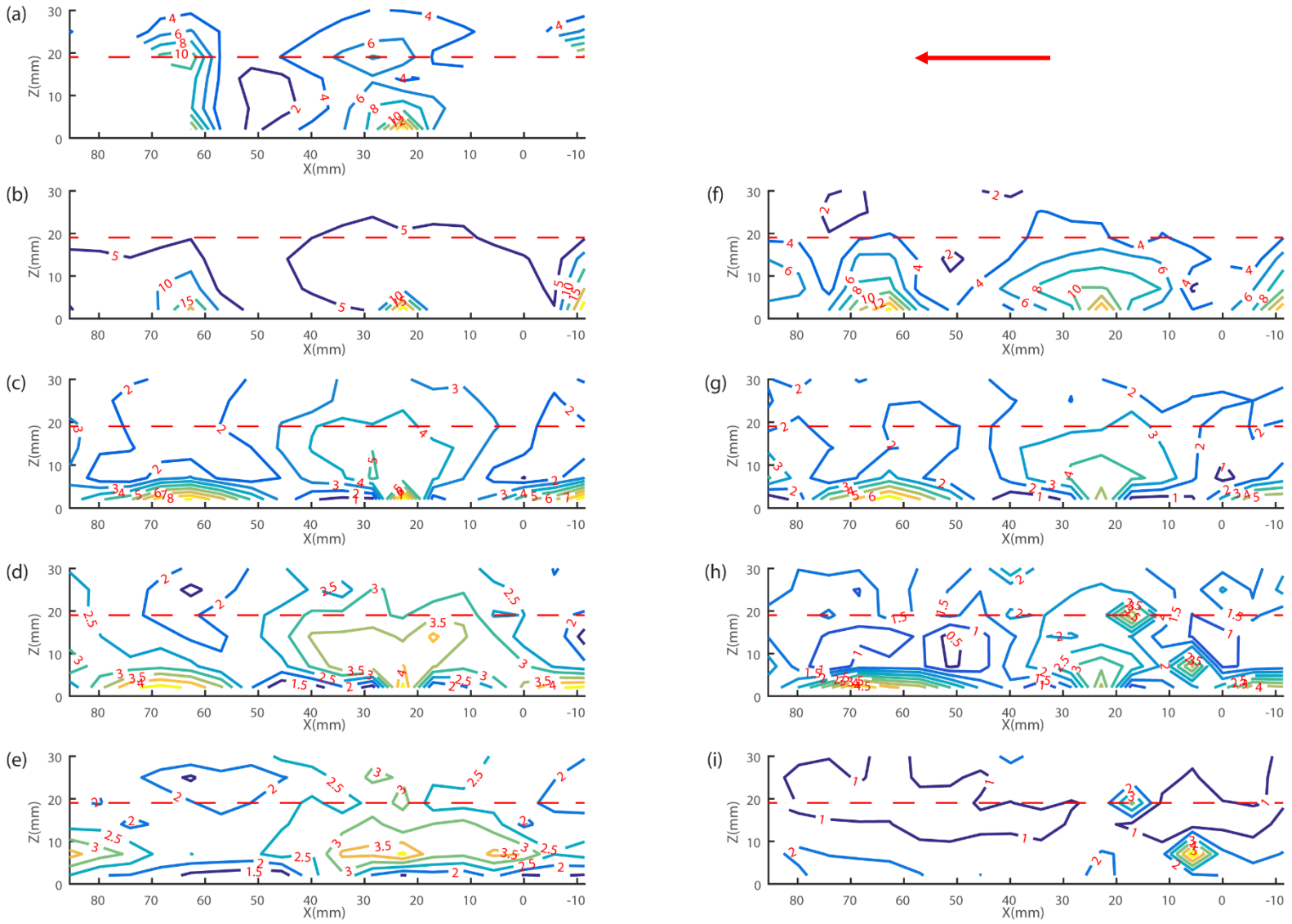

Figure 4.19 Contours of the secondary flow intensity (%) in vertical planes at y equal to: (a) 0; (b) 13.5; (c) 22.5; (d) 27; (e) 31.5; (f) -13.5; (g) -22.5; (h) -27; (i) -31.5 mm. The results are for the intermediate type roughness. The primary flow is from left to right (the red arrow).

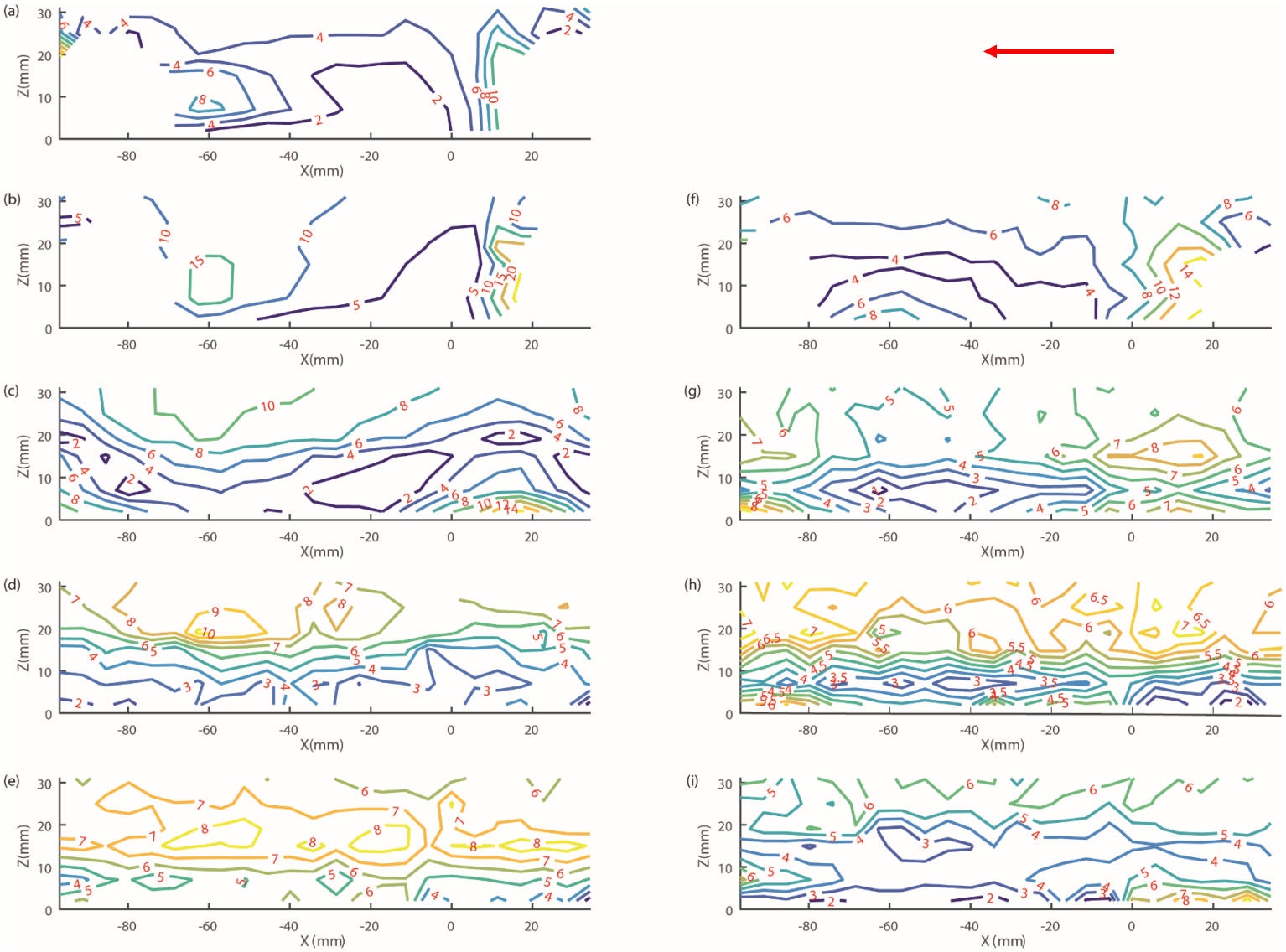

Figure 4.20 Contours of the secondary flow intensity (%) in vertical planes at y equal to: (a) 0; (b) 13.5; (c) 31.5; (d) 45; (e) 58.5; (f) -13.5; (g) -31.5; (h) -45; (i) -58.5 mm. The results are for the k-type roughness. The primary flow is from right to left (the red arrow)

4.4.3.2 Detailed structures of secondary flow for the d-type roughness

We examine the details of the secondary flow intensity, U_s, below. In Figure 4.18a, the contours show a region of strong U_s near the upstream face of the cube at downstream below the dashed line. This region is bounded by 5 mm $\leq z \leq$ 10 mm and 20 mm $\leq x \leq$ 24 mm. U_s decreases in the vertical direction, from 10 % at the elevation of z = 17 mm to 2% at z = 19 mm and to 6% at z = 2 mm, and in the negative x-direction from 10 % at x = 22 mm to 6% at x = 17 mm. These results are summarised in Table 4.8.

Table 4.8 Regions of relatively high secondary flow intensity at seven selected vertical sections of given y coordinates for the d-type roughness.

y	x	z	Maximum U_s	(x, z) of the maximum U_s	Figure
(mm)	(mm)	(mm)	(%)	(mm, mm)	
0	$20 \leq x \leq 24$	$5 \leq z \leq 10$	10	(22, 17)	4.18a
13.5	$14 \leq x \leq 25$	$2 \leq z \leq 6$	7	(17, 2)	4.18b
13.5	$38 \leq x \leq 42$	$2 \leq z \leq 6$	7	(40, 2)	4.18b
18	$12 \leq x \leq 24$	$2 \leq z \leq 4$	5	(27, 2)	4.18c
18	$-7 \leq x \leq 20$	$12 \leq z \leq 18$	3.5	(14, 15)	4.18c
18	$33 \leq x \leq 36$	$7 \leq z \leq 15$	3.5	(34, 10)	4.18c
22.5	$15 \leq x \leq 24$	$2 \leq z \leq 4$	6	(18, 2)	4.18d
22.5	$-6 \leq x \leq 14$	$7 \leq z \leq 17$	4	(4, 11)	4.18d
22.5	$34 \leq x \leq 40$	$8 \leq z \leq 15$	4	(46, 10)	4.18d
-13.5	$-2 \leq x \leq 9$	$10 \leq z \leq 17$	4.5	(4, 15)	4.18e
-13.5	$-6 \leq x \leq 14$	$7 \leq z \leq 17$	4	(34, 8)	4.18e
-18	$19 \leq x \leq 27$	$2 \leq z \leq 4$	4	(22, 2)	4.18f
-18	$x \leq 17$	$12 \leq z \leq 18$	4	z = 15	4.18f
-18	$17 \leq x \leq 29$	$12 \leq z \leq 18$	3.5	z = 15	4.18f
-18	$29 \leq x$	$12 \leq z \leq 18$	3.5	Z =15	4.18f
-22.5	$-8 \leq x \leq 4$	$2 \leq z \leq 6$	8	(-2, 2)	4.18g
-22.5	$15 \leq x \leq 24$	$2 \leq z \leq 8$	6	(18, 2)	4.18g

The vertical section at y = 13.5 mm (Figure 3.5) is shown in Figure 4.18b. This section is to the left (to an observer facing downstream) of the channel centreline (at y = 0), 3.5 mm off the left face (at y = 10 mm) of the central row of roughness elements. U_s is relatively high in two separate regions: one being downstream of the element at upstream, and the other near the left edge of the element at downstream. The coordinates of these regions, along with the local maximum values of U_s are summarised in Table 4.8. The vertical section at y = -13.5 mm (Figure 3.5) is shown in Figure 4.18e. This vertical section and that vertical section shown in Figure 4.18b are symmetrical about the channel centreline. Between these two sections, the secondary flow intensities are comparable above the dashed line, but they are not below. They differ not only in magnitude but also in structures. Quantitative comparisons are given in Table 4.8. The differences reflect the turbulent nature of flow over surface roughness.

The vertical section at y = 18 mm shown in Figure 4.18c and that at y = 18 mm shown in Figure 4.18f are symmetrical about the channel centreline (Figure 3.5). Above the dashed line, there are similarities in U_s between the two vertical sections. Below the dashed line, both sections show the same number of cores of relatively high U_s, although the locations of these cores do not match exactly. The bounding coordinates of the high U_s cores, along with the local maximum values of Us are listed in Table 4.8.

The vertical section at y = 25 mm (Figure 4.18d) and that at y = -25 mm (Figure 4.18f) are symmetrical about the channel centreline (Figure 3.5). Both sections show that the secondary flow intensity, U_s, is low above the dashed line, and that relatively high U_s is confined in the area below the dashed line. In both section, there is a region of relatively high U_s centred at x = 18 mm in the vicinity of the channel-bed. This is a similar feature of U_s distributions between Figures 4.18d and

4.18f. There are also similarities of U_s distributions below the dashed line between Figures 4.18d and 4.18c (Table 4.8).

We conclude that for the d-type roughness, the secondary flow has low intensities above the roughness height (or $z < h$, see Figures 2.1 and 3.4), and relatively high intensities below the roughness height. Relatively strong secondary flow is mainly located near the upstream face of a roughness element. Between some pairs of vertical sections symmetrical about the channel centreline (e.g. Figures 4.18c and 4.18f), the secondary flow has similar contour structures. Between other pairs, the flow has no similar structures, which means that the flow field is under the influence of other factors in addition to the surface roughness. These factors have contributed to the development of secondary flow at length scales larger than those associated with the roughness elements.

It is understood that the flow velocity (including secondary flow velocities) is zero at the solid channel-bed. A limitation of the measurements made in this experimental study is that the data points nearest to the bed are at the elevation of $z = 2$ mm from the bed. As shown in most of the vertical sections in Figures 4.18a–g, the secondary flow intensities at $z = 2$ mm are very high. The change from high intensities at $z = 2$ mm to zero intensity at the bed surface gives rise to a large velocity shear. Given the importance of velocity shear, it is desirable to obtain more data points within the short distance of 2 mm. However, obtaining more such data points has proven to be difficult.

4.4.3.3 Detailed structures of secondary flow for the intermediate type roughness

For the intermediate type roughness, the vertical section (Figure 4.19a) at the channel centreline (y = 0 mm, see Figure 3.7) shows that the secondary flow intensity, U_s, is strong in two regions. Their locations, along with the local maxima of U_s are listed in Table 4.9. One of them is near the bed, bounded by 2 mm ≤ z ≤ 25 mm and 18 mm ≤ x ≤ 30 mm. The local maximum intensity is U_s = 12% at (x, z) = (23 mm, 2 mm). The other is bounded by 2 mm ≤ z ≤ 22 mm and 60 mm ≤ x ≤ 64 mm, with a local maximum value of U_s = 10% at the elevation of z = 19 mm.

The vertical section shown in Figure 4.19b is located at y = 13.5 mm to the left of the channel centreline (Figure 3.7), about 3.5 mm from the left face of the central row of roughness elements. The contours of U_s in Figure 4.19b show three regions of strong U_s, which are listed in Table 4.9. The vertical section (at y = -13.5 mm) shown in Figure 4.19f and that in Figure 4.19b are symmetrical about the channel centreline. Two regions of strong U_s appear below the roughness height in Figure 4.19f, which are similar to two of the three regions of strong U_s in Figure 4.19b, as compared in Table 4.9. Above the roughness height, the secondary flow intensities are lower in Figure 4.19f than Figure 4.19b.

Between the vertical section at y = 22.5 mm (Figure 4.19c) and that at y = -22.5 mm (Figure 4.19g), contours of U_s are similar. The main features are the existence of three regions of relatively high U_s below the roughness height. The locations of these regions relative to the roughness elements at upstream and at downstream, along with local maxima of U_s are listed in Table 4.9.

Table 4.9 Regions of relatively high secondary flow intensity at ten selected vertical sections of given y coordinates for the intermediate type roughness.

y	x	z	Maximum U_s	(x, z) of the maximum U_s	Figure
(mm)	(mm)	(mm)	(%)	(mm, mm)	
0	$18 \le x \le 30$	$2 \le z \le 25$	8	(23, 2)	4.19a
0	$18 \le x \le 30$	$2 \le z \le 25$	8	(28, 19)	4.19a
0	$60 \le x \le 64$	$2 \le z \le 22$	10	(64, 19)	4.19a
13.5	$19 \le x \le 26$	$2 \le z \le 5$	15	(23, 2)	4.19b
13.5	$-11.4 \le x \le -6$	$2 \le z \le 10$	15	(-10, 2)	4.19b
13.5	$60 \le x \le 66$	$2 \le z \le 5$	15	(63, 2)	4.19b
22.5	$-11.4 \le x \le -5$	$2 \le z \le 5$	8	(-10, 2)	4.19c
22.5	$20 \le x \le 25$	$2 \le z \le 5$	8	(23, 2)	4.19c
22.5	$56 \le x \le 73$	$2 \le z \le 5$	8	(64, 2)	4.19c
27	$-11.4 \le x \le 0$	$2 \le z \le 5$	4	$z = 2$	4.19d
27	$23 \le x \le 21$	$2 \le z \le 8$	4	(22, 2)	4.19d
27	$60 \le x \le 76$	$2 \le z \le 4$	4	(69, 2)	4.19d
31.5	$0 \le x \le 35$	$5 \le z \le 10$	3.5	(28, 7)	4.19e
31.5	$0 \le x \le 35$	$5 \le z \le 10$	3.5	(5, 7)	4.19e
-13.5	$-11.4 \le x \le -7$	$2 \le z \le 6$	12	(-11.4, 2)	4.19f
-13.5	$26 \le x \le 20$	$2 \le z \le 6$	12	(24, 2)	4.19f
-13.5	$61 \le x \le 69$	$2 \le z \le 6$	14	(64, 2)	4.19f
-22.5	$-11.4 \le x \le -1$	$2 \le z \le 5$	5	(-10, 2)	4.19g
-22.5	$22 \le x \le 24$	$2 \le z \le 5$	5	(23, 2)	4.19g
-22.5	$54 \le x \le 74$	$2 \le z \le 5$	6	(63, 2)	4.19g
-27	$-11.4 \le x \le -1$	$2 \le z \le 5$	4	$z = 2$	4.19h
-27	$4 \le x \le 9$	$5 \le z \le 10$	3.5	(6, 8)	4.19h
-27	$13 \le x \le 20$	$18 \le z \le 21$	3.5	(18, 19)	4.19h
-27	$21 \le x \le 24$	$2 \le z \le 7$	4	(22, 2)	4.19h
-27	$53 \le x \le 75$	$2 \le z \le 4$	4.5	(65, 2)	4.19h
-31	$2 \le x \le 9$	$4 \le z \le 10$	5	(6, 8)	4.19i
-31	$14 \le x \le 19$	$18 \le z \le 21$	3.5	(18, 19)	4.19i

In Figure 4.19d, contours of U_s in the vertical plane at y = 27 mm are plotted. The contours show similar structures to those in Figure 4.19c, with three regions of relatively high U_s below the roughness height. The locations of these regions as well as local maxima of Us are listed in Table 4.9. The vertical section shown in Figure 4.19h is symmetrical with that shown Figure 4.19d. Overall, the secondary flow intensities are lower in the former than in the latter. However, there are similarities in regions of relatively high U_s near the channel-bed between the two vertical sections, as compared in Table 4.9.

Contours of U_s in the vertical section at y = 31.5 mm (Figure 3.7) are plotted in Figure 4.19e. This vertical section is at about 11.5 mm to the left of the left face of the central row of roughness elements. The secondary flow intensities are generally low. This is also the case in the vertical section at y = -31.5 mm (Figure 4.19i). The roughness elements have little contribution to the generation of secondary flow in these two vertical sections.

4.4.3.4 Detailed structures of secondary flow for the k-type roughness

With regards to the secondary flow intensity, U_s, for the k-type roughness, we make the following observations:

- The intensities (Figures 4.20a–i) are much stronger than those for the d-type roughness (Figures 4.18a–g) and for the intermediate type roughness (Figures 4.19a–i). This means that the k-type roughness are more effective in producing secondary flow than the other two types of roughness.
- There is a lack of symmetry of secondary flow intensity between pairs of vertical sections that are symmetrical about the channel centreline. For example, the vertical sections shown in Figures 4.20b and 4.20f are symmetrical, but the U_s distributions are different in both

magnitude and structures between the two vertical sections. This is also true between other symmetrical sections (Figures 4.20c and 4.20g; Figures 4.20d and 4.20h; Figures 4.20e and 4.20i). This is possibly due to the spacing between adjacent roughness elements (Figure 3.6) is large enough for the open-channel flow to develop and behave in an irregular manner.

- The vertical sections shown in Figures 4.20b–e are located at increasing lateral distances (3.5, 21.5, 35, and 48.5 mm, respectively) from the left face of the central row of roughness elements. Among these figures, the secondary flow intensities are the highest in Figure 4.20b, and the lowest in Figure 4.20e. Similar comparisons are seen from Figures 4.20f–i for vertical sections to the right of the right face of the central row of roughness elements. We conclude that the individual roughness elements produce secondary flow when the primary flow approaches them and the intensity of secondary flow decays with an increasing distance from the elements.

Chapter 5 Conclusions

5.1 Concluding remarks

This thesis reports laboratory measurements of three-dimensional (3-D) velocities of turbulent flow over roughness elements at the bed of an open-channel. The measurements were made from flume experiments using an acoustic Doppler velocimeter. The focus of the work is on the flow field near the bed. The configurations of roughness elements used cover the d-type, intermediate type, and k-type roughness. The following conclusions have been reached:

1) A large volume of turbulent flow velocity measurements at accurate positions in the near-bed region has been obtained. Such measurements are rarely available from the literature.
2) Analysing the measurements has led to the identification of a variety of vertical profiles of the mean longitudinal velocity. These profiles show different shapes: a) The simplest shape is a straight line throughout the water column; b) The next level of complexity is two portions of equal number of data points that are collinear; c) A more complex shape is a combination of linear with nonlinear portions; d) Some profiles are purely nonlinear variations, with a sudden increase in velocity immediately from the bed; e) Other profiles show flow separation from the bed. These results are new. Some profile shapes are similar to the field measurements from rivers discussed in Byrd et al. (2000).
3) The widely used logarithmic velocity distribution is not adequate to describe the measured mean velocity profiles in the majority of the cases. Even the d-type surface roughness cannot simply be treated as a smooth surface; the measured near-bed velocities deviate substantially from logarithmic distributions.

4) The measured turbulent shear stress, τ, exhibits five different types of distributions. All are of nonlinear shapes when the entire water column is taken into account. Above the roughness height, Type 1 profiles show monotonically decreasing τ toward higher elevations from the bed. Type 2 profiles show a trend of monotonically increasing τ toward higher elevations. Type 3 profiles show essentially constant τ values. Type 4 profiles show a local maximum of τ above the roughness height. Type 5 profiles show a local minimum of τ above the roughness height. Below the roughness height, the variations of τ have different patterns including linear variations, weakly nonlinear variations, and zig-zag variations.
5) Estimates of the bed shear stress using the law-of-the-wall contain large errors for turbulent flow under the rough surface conditions investigated in this experimental work.
6) The k-type roughness produces much higher secondary intensities than the intermediate type and d-type roughness. The d-type roughness is the least effective in producing secondary flow.
7) For the k-type roughness, there is a lack of symmetry of secondary flow intensity between a pair of vertical sections that are symmetrical about the channel centreline. This is possibly due to the spacing between adjacent roughness elements is large enough for the flow to develop and behave in an irregular manner. An individual k-type roughness element produces secondary flow when the primary flow approaches it and the intensity of secondary flow decays with an increasing distance from it.
8) For all the roughness types, the secondary flow intensities are higher below the roughness height than above. Within the cavity space between adjacent roughness elements, there are large spatial variations in the secondary flow intensities, as summarised in Tables 4.2–4.9.

9) In this study, the data points nearest to the bed are at the elevation of 2 mm from the channel-bed. This is a limitation. Our measurements show that secondary flow intensities at this elevation are still very high. The change from high intensities at this elevation to zero intensity at the bed surface gives rise to a large velocity shear. It is desirable to obtain more data points within the short distance of 2 mm. However, obtaining more such data points has proven to be difficult.

5.2 Suggestions for future studies

Future studies of the topic of turbulent open-channel flow over roughness surface should consider the following:

- The aspect ratio of a channel (or the ratio of channel width to flow depth) is known to produce effects of the development of secondary flow. At a low aspect ratio, the artificial effect of the presence of channel sidewalls is significant. Future studies should perform experiments in flume channels with a large aspect ratio. The results from such experiments will not suffer a significant sidewall effect.
- To a certain degree, placing an ADV in the flow disturbs the flow field and thus creates artificial effects. Future studies can use nonintrusive technology (e.g. laser Doppler anemometer) for measurements of flow velocity to avoid the artificial effects.
- Experiments are time consuming and incur high costs. Future studies should implement numerical modelling to extend experimental results and to explore sensitivity of the flow field to changes in roughness element configurations, approach flow conditions, and the Froude number.

References

Agelinchaab, M. and Tachie, M.F., 2006. Open channel turbulent flow over hemispherical ribs. *International Journal of Heat and Fluid Flow*, *27*(6), pp.1010-1027.

AS Nortek, *Comprehensive Manual*, 2013, [online] Available: http://www.nortek-as.com/lib/manuals/the-comprehensive-manual.

Byrd, T.C., Furbish, D.J. and Warburton, J., 2000. Estimating depth-averaged velocities in rough channels. *Earth Surface Processes and Landforms: The Journal of the British Geomorphological Research Group*, *25*(2), pp.167-173.

Cameron, S., Nikora, V. and Coleman, S., 2008. Double-averaged velocity and stress distributions for hydraulically-smooth and transitionally-rough turbulent flows. *Acta Geophysica*, *56*(3), pp.642-653.

Coleman, S.E., Nikora, V.I., McLean, S.R. and Schlicke, E., 2007. Spatially averaged turbulent flow over square ribs. Journal of Engineering Mechanics, 133(2), pp.194-204.

Goring, D.G. and Nikora, V.I., 2002. Despiking acoustic Doppler velocimeter data. Journal of Hydraulic Engineering, 128(1), pp.117-126.

Jesson, M.A., Bridgeman, J. and Sterling, M., 2015. Novel software developments for the automated post-processing of high volumes of velocity time-series. Advances in Engineering Software, 89, pp.36-42.

Jiménez, J., 2004. Turbulent flows over rough walls. *Annu. Rev. Fluid Mech.*, *36*, pp.173-196.

Li, J. and Li, S.S., 2018. Discussion of "Turbulence over cube-mounted rough bed using spatiotemporal averaging approach". *Canadian Journal of Civil Engineering*, (999), pp.1-2.

Manes, C., Pokrajac, D. and McEwan, I., 2007. Double-averaged open-channel flows with small relative submergence. *Journal of Hydraulic Engineering*, *133*(8), pp.896-904.

Perry, A.E., Schofield, W.H. and Joubert, P.N., 1969. Rough wall turbulent boundary layers. *Journal of Fluid Mechanics*, *37*(2), pp.383-413.

Schlichting, H. and Gersten, K., 2016. *Boundary-layer theory*. Springer.

Singh, S.K., Debnath, K. and Mazumder, B.S., 2017. Turbulence over cube-mounted rough bed using spatiotemporal averaging approach. *Canadian Journal of Civil Engineering*, *44*(7), pp.504-517.

Te Chow, V., 1959. Open-channel hydraulics (Vol. 1). New York: McGraw-Hill.

Wang, X.K., Ye, C., Wang, B.J. and Yan, X.F., 2015. Experimental study on velocity profiles with different roughness elements in a flume. *Acta geophysica*, *63*(6), pp.1685-1705.

Wilcox, D.C., 2006. Turbulence modeling in CFD, 3rd edn La Canada, CA: DCW Industries.